Photocatalytic CO₂ Conversion Using Metal-Containing Coordination Polymers and Networks: Recent Developments in Material Design and Mechanistic Details

Lea-Sophie Hornberger [1] **and Friederike Adams** [1,2,*] (ID)

1   Chair of Macromolecular Materials and Fiber Chemistry, Institute of Polymer Chemistry, University of Stuttgart, Pfaffenwaldring 55, 70569 Stuttgart, Germany; lea-sophie.hornberger@ipoc.uni-stuttgart.de

2   Center for Ophthalmology, University Eye Hospital Tübingen, Elfriede-Aulhorn-Strasse 7, 72076 Tübingen, Germany

*   Correspondence: friederike.adams@ipoc.uni-stuttgart.de; Tel.: +49-711-68564488

Abstract: International guidelines have progressively addressed global warming which is caused by the greenhouse effect. The greenhouse effect originates from the atmosphere's gases which trap sunlight which, as a consequence, causes an increase in global surface temperature. Carbon dioxide is one of these greenhouse gases and is mainly produced by anthropogenic emissions. The urgency of removing atmospheric carbon dioxide from the atmosphere to reduce the greenhouse effect has initiated the development of methods to covert carbon dioxide into valuable products. One approach that was developed is the photocatalytic transformation of CO₂. Photocatalysis addresses environmental issues by transferring CO₂ into value added chemicals by mimicking the natural photosynthesis process. During this process, the photocatalytic system is excited by light energy. CO₂ is adsorbed at the catalytic metal centers where it is subsequently reduced. To overcome several obstacles for achieving an efficient photocatalytic reduction process, the use of metal-containing polymers as photocatalysts for carbon dioxide reduction is highlighted in this review. The attention of this manuscript is directed towards recent advances in material design and mechanistic details of the process using different polymeric materials and photocatalysts.

Keywords: photocatalysis; CO₂ conversion; carbon dioxide reduction; artificial photosynthesis; metal-containing polymers; metallopolymers; porous organic polymers; porous coordination polymers; metal-organic frameworks; metal-organic layers

1. Introduction

In 2015, the United Nations stated 17 Sustainable Development Goals to fight climate change. Sustainable Development Goal 13 contains the mission of climate action: Adapting to climate change and investing in low-carbon development [1]. The mission started by dramatically decreasing greenhouse gas (GHG) emissions. Carbon dioxide is one of the GHGs, evolving from natural processes, but mainly from artificial activities. The amount of CO₂ in the atmosphere has notably risen from the beginning of the industrial era and is steadily increasing. In 1750, at the beginning of the industrial revolution, the CO₂ concentration in the atmosphere was 277 parts per million (ppm) [2] and has expanded to up to over 400 ppm measured in May 2022 [3].

Four different approaches can lead to a reduction in CO₂ in the atmosphere: (1) Improving energy efficiencies in general, (2) use of energy sources that have zero or lower carbon dioxide exhaust such as solar or wind resources, (3) capturing the atmospheric CO₂ geologically or (4) converting CO₂ into valuable materials [4]. Conversion of carbon dioxide faces a number of hurdles since CO₂ is the final product of carbon combustion and is a relatively inert gas. The reduction potential of CO₂ vs. the Normal Hydrogen Electrode (NHE) E^0 is −1.9 V, showing that in an electrochemical process, conversion

demands high energy caused by high overpotential for a reaction taking place [5]. To overcome this drawback, catalysts are used to enable the economic conversion of CO_2 into fuels and chemicals. Transforming atmospheric CO_2 into C1/C2 fuels and other valued chemicals, such as carbon monoxide, methanol, formic acid, or methane, is a sustainable strategy for global carbon balance [6–10].
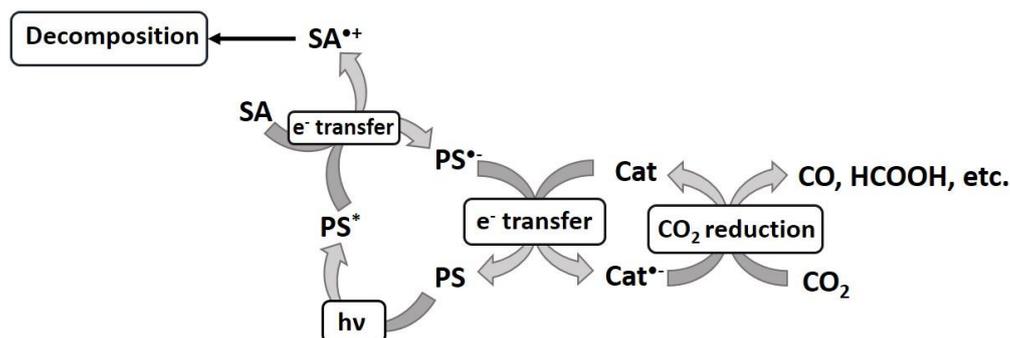
This review focusses on metal-containing polymers as catalysts for photochemical CO_2 conversion. Nowadays, metal-containing polymers, also known as metallopolymers, are at the forefront for discovering new and sustainable homogeneous, as well as heterogeneous, catalysts. The combination of metal and polymer moieties merges the advantage of both materials: Metal centers build up the functional core as redox-active species, whereas polymeric materials are able to optimize the catalyst performance while acting as stabilizing structures due to their feature of being tunable. Especially for carbon dioxide conversion, metal-containing polymers can support photocatalytic [11–15], electrocatalytic [16–20], photo-electrocatalytic [13,15,21–23] or thermochemical [24] reduction reactions.

A photocatalytic reduction system comprises different components, namely, a catalyst, a photosensitizer and an electron sacrificing agent. Photosensitizers (PS) offer the ability to absorb light in the visible region and form electron-hole pairs. Sacrificial agents (SA) work as electron donors by reducing the photosensitizer [25,26]. This process scales down the recombination of electron and holes. That means that the redox potentials of the sacrificial agents and the photosensitizer have to be in accordance with each other. The photosensitizer is the species in the system that absorbs most of the light. The longevity of the excited state of the PS is required to be high enough to be reduced by the sacrificial agent. Therefore, organometallic photosensitizers consisting of metal atoms as the center combined with organic ligands, such as $[Ru(bpy)_3]^{2+}$ with 2,2′-bipyridine (bpy) ligands, were used. Water was mostly utilized as a sacrificial hole scavenger and solvent. However, oxidation from water to O_2 required four electron holes (Table 1) and the generated O_2 could act as an oxidizing agent having an adverse effect on the reduction reaction [27]. Therefore, organic substances were used as additional sacrificial agents, i.e., triethanolamine (TEOA), triethylamine (NEt_3 or TEA), 1-benzyl-1,4-dihydronicotinamide (BNAH) or 1,3-dimethyl-2-phenyl-2,3-dihydro-1H-benzo[d]imidazole (BIH) [28].

After reduction by the SA, the photosensitizer can transfer the electron to the catalyst and return to the ground state. The metal center must be an electron-rich metal atom with filled d-orbitals as found in second- or third-row metals such as ruthenium or rhodium [25]. Organic ligands provide π-electron-accepting units for metal-to-ligand charge transfer (MLCT). The strong spin-orbit coupling in the second- or third-row metals enabled a pathway for excited electrons that switch multiplicities through intersystem crossing (ISC) [29,30]. Besides receiving electrons from the photosensitizer, the catalytic species needs to accumulate the electrons for facilitating the multi-electron reduction of CO_2. For this purpose, CO_2 needs to be adsorbed on the catalytic center. Metalorganic complexes are used with Mn(I), Re(I), Ru(II), Co(II), Ni(II), Ir(III) and Fe(III) transition metal centers that can coordinate carbon dioxide [25]. The surface adsorption activates the CO_2 molecules and forms partially charged $CO_2^{\delta\bullet-}$ species. CO_2 adsorption occurs via oxygen coordination, carbon coordination or mixed coordination. Either the oxygen atoms coordinate with their electron lone pairs by donating them to Lewis acid centers on the surface, the carbon accepts electrons from a Lewis base, or a mixed coordination of both processes happens. Adsorbed $CO_2^{\delta\bullet-}$ molecules are no longer linear and have a bended structure [31]. After the catalyst assembles the electrons, these are transferred to CO_2, which is reduced to give the reduction products, such as carbon monoxide, formic acid or methane (Scheme 1).

The whole process can be optimized by tuning the band energy of the light absorbing molecule. The light energy needs to be higher than its band gap to provide the required energy. Therefore, the photons of sunlight are divided up according to their energies/wavelengths into photons in the ultraviolet light range ($\lambda < 400$ nm, $E_{photon} > 3.1$ eV), visible light range ($\lambda = 400$–700 nm, $1.7 \leq E_{photon} \leq 3.1$ eV), and infrared light range

($\lambda > 400$ nm, $E_{\text{photon}} < 1.7$ eV). The sunlight consists of 95% visible and infrared irradiation [32]. To be able to absorb light in this range, the band gap of the photocatalytically active materials is designed to be smaller than 3.1 eV. The band gap can not only be tuned for favorable light absorption but can also be adjusted for suitable potentials for subsequent redox reactions. The conductive band (CB) of the photocatalyst needs to be raised to a level which is higher than the reduction potential of CO_2, while the valence band (VB) must exceed the oxidation potential of the electron donor in energy [14]. The reactions to the different products have distinct potentials. Table 1 presents the half-cell reactions and their appropriate potentials vs. the normal hydrogen electrode (NHE) at pH = 7 ($E^{0\prime}$) [33,34].

Scheme 1. Basic mechanism for the photocatalytic CO_2 reduction including sacrificial agent (SA), photosensitizer (PS) and catalyst (Cat). Data from Refs. [25,26].

Table 1. Half-cell reactions and potentials vs. the NHE at pH = 7 [33,34].

Half-Cell Reaction	$E^{0\prime}$ in V
$2\,H_2O \rightarrow O_2 + 4\,H^+ + 4\,e^-$	$+0.82$
$2\,H^+ + 2\,e^- \rightarrow H_2$	-0.41
$CO_2 + 2\,H^+ + 2\,e^- \rightarrow CO + H_2O$	-0.52
$CO_2 + 2\,H^+ + 2\,e^- \rightarrow HCOOH$	-0.61
$CO_2 + 4\,H^+ + 4\,e^- \rightarrow C + 2\,H_2O$	-0.20
$CO_2 + 4\,H^+ + 4\,e^- \rightarrow HCHO + H_2O$	-0.48
$CO_2 + 6\,H^+ + 6\,e^- \rightarrow CH_3OH + H_2O$	-0.38
$CO_2 + 8\,H^+ + 8\,e^- \rightarrow CH_4 + 2\,H_2O$	-0.24

In 1982, Lehn and Ziessel published one of the first innovative studies on the photochemical generation of carbon monoxide and hydrogen from CO_2 and H_2O. The authors used $Ru(\text{bipyridine})_3{}^{2+}$ as the photosensitizer, Co^{2+} as the reducing intermediate/catalyst, and NEt_3 as the electron donor dissolved in an aqueous acetonitrile solution. The addition of bipyridine affected the amount and ratio of generated gas. Lehn and Ziessel proposed an intermediate formation of Co(I) species in a reduction system together with $[Ru(bpy)_3]^{2+}$, but its nature was unknown at that point. It was only known that Co acted as a binder as well as an electrocatalyst for CO_2 reduction [34]. Since then, interest in systems for CO_2 photoreduction reaction has continuously grown due to their advantages over other methods: (1) The whole process is controllable and can be carried out under mild conditions in matters of reaction temperature and pressure; (2) when catalysts are completely recyclable, the overall consumption of all substances can be minimized, resulting in solely small molecule and atmospheric CO_2 consumption; (3) the light source can be chosen individually by applying, e.g., renewable resources such as solar energy, and (4) the systems are modular and can easily be scaled-up [4,35,36].

However, the mechanistic details for photocatalytic CO_2 reduction including photosensitizer and sacrificing agents in the mechanistic circles are complex and mechanistic investigations are still ongoing. On the other hand, research on material design and efficiencies is simultaneously continuing to grow. The number of publications on photocatalytic

carbon dioxide reduction exponentially increased up to 12,800 publications in the year 2021 alone (Figure 1). Additionally, publications on photocatalytic carbon dioxide reduction including polymers exponentially increased to 5790 in 2021, showing the high potential of polymers for assisting carbon dioxide conversion.
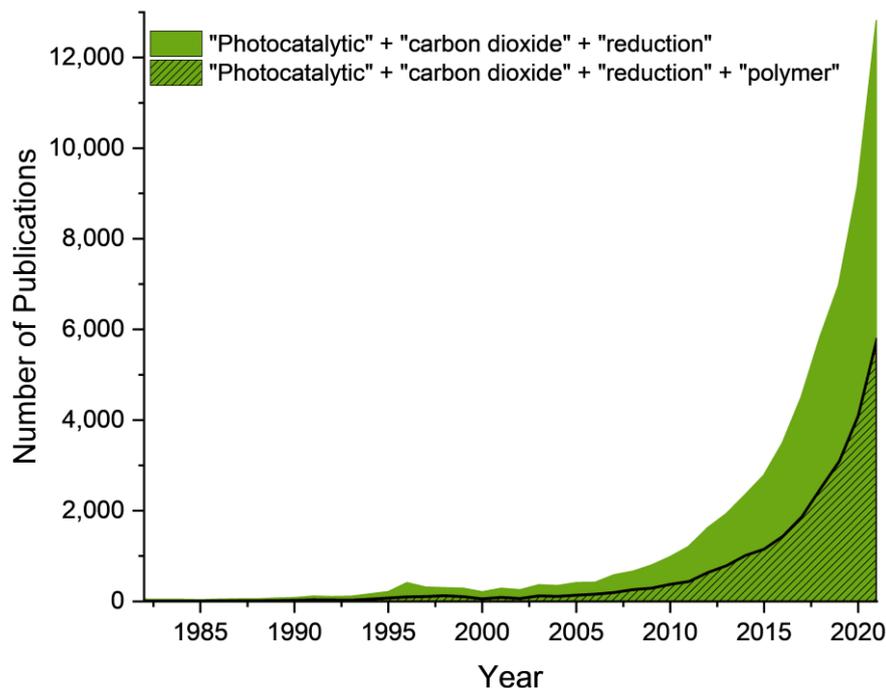

Figure 1. Publications per year between 1982 and 2021 that include the words "photocatalytic", "carbon dioxide", "reduction", and "polymers". Source: Google Scholar (Status: May 2022).

Challenges have emerged for photocatalysts in their performance due to low CO_2 adsorptions, conversion efficiencies, and selective product generation [11,36–38]. Additionally, most of the photocatalytic systems lack stability, as it was revealed in several studies that a catalyst can barely be used for several catalytic cycles [11,36]. Stability issues caused by charges also influence the efficiency, showing that electrons and holes have to be separated adequately within the material to enhance stability. Moreover, the light absorption range is often limited and efforts need to be made to adjust this range to be in the visible light region. To sum up the requirements for photocatalytic systems: (1) suitable band gaps, (2) light absorption abilities in a broad range, (3) the efficient charge separation of electrons and holes, and (4) several adsorptive as well as reactive sites.

Recent advances have been made to overcome these obstacles such as new tailor-made materials combining photocatalysts and polymeric materials, which are summarized in this review article. As the number of materials for CO_2 reduction is enormous, this manuscript focusses on recent developments in metal-containing polymeric systems. Different classes of 1D-coordination polymers and 2D-/3D-coordination networks, including supramolecular and coordination polymers, porous organic frameworks and metal-organic frameworks (MOFs) as photocatalysts, in addition to further strategies, are presented. Despite ongoing discussion regarding whether metal-organic frameworks can be considered as 3D-coordination polymers [39], we herein define MOFs and covalent organic frameworks (COFs) as coordination networks, a sub-category of coordination polymers, as also recommended by IUPAC [40].

2. 1D-Coordination Polymers

2.1. Re/Ru-Systems

In 2018, Rieger et al. published a micellar support for Re-metal complexes for CO_2 reduction. They were the first to use an end group-functionalized polymer for the selec-

tive complexation of a rhenium complex. The authors synthesized a block copolymer via yttrium-mediated group-transfer polymerization (GTP) using hydrophobic 2-vinylpyridine (2VP) and hydrophilic diethyl vinylphosphonate (PDEVP) as monomers. AB-block copolymers (A = poly(2-vinylpyridine) (P2VP), B = poly(diethyl vinylphosphonate) (PDEVP)) were end-group functionalized with *ortho*-methylated bipyridines which were introduced as initiators of the yttrium catalysts. The photosensitizer and photocatalyst [Re(CO)$_3$(bpy)Cl] was attached to the end-groups by complexation to yield Re-bpy-P2VP-PDEVP-block copolymers. Dynamic light scattering showed the ability of the polymers to self-assemble to micelles with tunable sizes dependent on the polymer chain lengths while protecting the Re-metal center in the micellar core. The systems were tested as photocatalysts for CO$_2$ reduction in *N,N*-dimethylformamide (DMF) with TEOA as the sacrificial electron donor under LED light irradiation. In comparison to the respective molecular catalyst, the complexation to a P2VP-PDEVP-block copolymer structure increased the catalytic performance, producing CO as the exclusive product with a turnover number (TON) of 13 containing a 0.1 mM catalyst. The pure catalyst itself showed a TON of 6.5 in the same setup. It was proven that the attachment of a metal complex did not limit the catalytic properties and even enhanced them, resulting in higher TONs [41].

Since water is the most abundant and ecological solvent, in 2022, He et al. introduced the first visible light-induced material for photocatalytic CO$_2$ reduction in aqueous media without the need for the addition of any further photosensitizer. The authors used triblock amphiphilic micelles which are able to self-assemble in water. The polycarbonate-based triblock polymeric micelles contained a rhenium complex in the backbone, namely Re(dcbpy) (dcbpy = 2,2′-bipyridine-5,5′-dicarboxylic acid), as a photocatalyst [42]. The material was synthesized by the copolymerization of CO$_2$ and epoxide, followed by subsequent thiol-ene click reactions according to a previous publication [43]. In detail, tris-carbonylbromo(2,2′-bipyridine-5,5′-dicarboxylic acid) rhenium(I) (RETC) was synthesized by mixing [Re(CO)$_5$Cl] and the bipyridine compound H$_2$BPYDC, followed by the synthesis of the Re-hydrophobic polymer (RETC-HP) with bifunctional RETC as a chain transfer agent and propylene oxide (PO) as a monomer unit (Figure 2). Triblock Re-polymers (RETC-TB) were produced by using allyl glycidyl ether (AGE) as the second block. Thiol-ene click reaction of the RETC-TB with thioglycolic acid resulted in an amphiphilic Re-polymer (RETC-AP). Transmission electron microscopy (TEM) measurements of RETC-AP displayed spherical micelles with uniform particle sizes in water. The micelles had a core–shell structure with the hydrophilic polymer blocks in the outer sphere. The Re-functionality was protected in the hydrophobic core part. Polycarbonate chains suppressed dimerization of Re to maintain its activity. The functionality, as well as the morphology and porosity of the amphiphilic polycarbonate micellar rhenium catalysts, were easily regulated by the size of the hydrophilic and hydrophobic blocks. Photoreductions of CO$_2$ were performed in water with TEOA as a sacrificial agent. Only CO and H$_2$ were detected as products. CO selectivity was higher than 99% and the TON could be boosted to be 110, which is 37 times higher compared to the molecular Re catalyst in the organic solvent [42].

The newest approach by Rieger et al. took advantage of Lewis pair mediated GTP with different Lewis acidic trialkyl aluminum compounds and Lewis basic phosphines to result in well-defined polymers with bipyridine monomer units for Re- and Ru-complexation. 4-Vinyl-4′-methyl-2,2′-bipyridine (VBpy) was catalytically polymerized for the first time and a combination of Al(*i*-BU)$_3$ and PMe$_3$ was determined as the optimum combination as a catalyst for polymerization. A two-step synthesis was performed to load the bipyridine bearing polymers, first with [Re(CO)$_5$Cl] as the catalytic centers, followed by Ru(dmb)$_2$Cl$_2$ (dmb = 4,4′-dimethyl-2,2′-bipyridine) performing as a photosensitizer to give macromolecular rhenium-ruthenium complexes (Figure 3). In comparison to earlier studies, multiple bipyridine units were available in the polymer and not solely the end-group/initiating species was utilized. Polymer-complex structures were characterized by ultraviolet–visible (UV-vis), photoluminescence (PL) and infrared (IR) spectroscopy, as well as by inductively coupled plasma mass spectrometry (ICP-MS). The photocatalytic activity was measured

under visible light irradiation in DMF with the addition of TEOA as the base and BIH as the sacrificial electron donor. Attachment of the rhenium and ruthenium centers to the poly(vinyl bipyridine) (PVBpy) offered proximity to these metal centers for an enhanced intramolecular electron transfer. PVBpy with a photocatalyst-to-photosensitizer ratio of 5% Re(I) compared to 95% Ru(II) showed a TON of 6088 and a turnover frequency (TOF) of 66 h^{-1} for the conversion of CO_2 to CO due to effective electron transfers from the one electron reduced Ru(II) to the Re(I) centers [44].
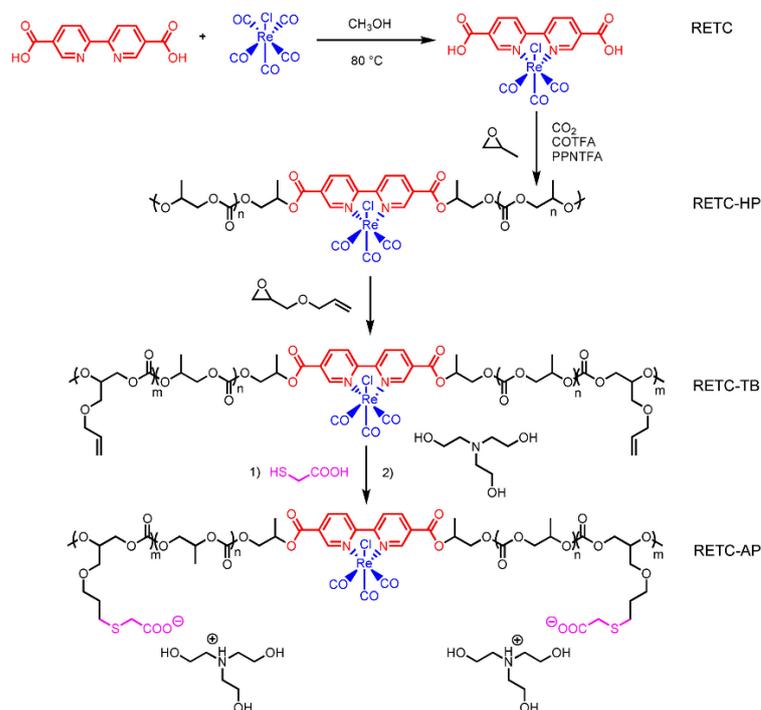

Figure 2. Synthesis of Re(dcbpy)-based amphiphilic micellar catalysts, starting from Re(dcbpy)(CO)$_3$Cl (RETC) via Re-hydrophobic polymer (RETC-HP) and triblock Re-polymer (RETC-TB) resulting in Re-amphiphilic polymer (RETC-AP). Reprinted with permission from Ref. [42]. Copyright 2022, Wiley-VCH.
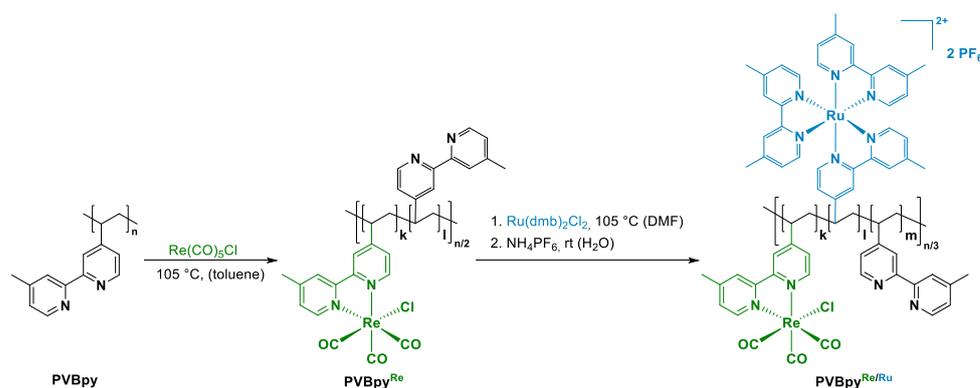

Figure 3. Two-step synthesis of the PVBpy$^{Re/Ru}$ photocatalyst by loading with Re(CO)$_5$Cl and Ru(dmb)$_2$Cl$_2$ [44].

Kim and Choi reported a molecular photosensitizer-catalyst assembly without the need of any chemical linkage, since linking the photosensitizer and the catalyst could require complex synthesis procedures. It can also cause disadvantages due to the close interactions of the functional centers on the one hand but prevents catalyst leaching on the other hand. Therefore, the authors utilized a Nafion polymer backbone (Nf) as

a platform for attaching the photosensitizer and catalyst by electrostatic attraction [45]. Nafion ionomers were synthesized by the copolymerization of a perfluorinated vinyl ether comonomer with tetrafluoroethylene (Figure 4) [46]. The light absorber $[Ru(bpy)_3]^{2+}$ (RuL) and the catalyst *fac*-Re(bpy)(CO)$_3$Cl:Re(I) (Re(I)) were both physically assembled on the Nafion platform in DMF. Re(I) was attached via hydrophobic interactions, as shown by infrared spectroscopy in the solid state. Washing with DMF proved only a weak bonding by physical interactions because Re(I) was easily washed away. RuL was linked in a stronger way via ionic interactions between the cationic RuL and the anionic sulfonic Nf group to form RuL-Nf. The binding was further characterized by monitoring the absorbance. UV-vis spectra of RuL-Nf in DMF showed that the Nf had no influence on the absorption characteristics of RuL. Photocatalytic reduction in carbon dioxide with Re(I)-RuL-Nf was tested in DMF with TEOA as the electron donor. CO production was analyzed by gas chromatography. RuL showed enhanced deactivation with higher RuL concentrations, indicating a self-sensitizing destruction. Upon excitation, the excited RuL* either reacted with the electron donor, or with itself by a self-destructive process. The role of the Nf was suggested to hinder this self-destruction and thus maintain the photoactivity and durability of the RuL photosensitizer. After reaction with TEOA, the excited and reduced RuL transferred its electron to the Re(I) followed by CO_2 reduction to CO. The TON of Re(I)-RuL-Nf was calculated to be up to 454 after 10 h. This value was four times higher than the TON of 110 when using the molecular Re(I)-RuL catalytic system without Nafion fixation, proving the increased efficiency when using a Nafion backbone. Additionally, the presence of water dramatically decreased the photocatalytic reduction implying that water is not needed as a proton donor [45].
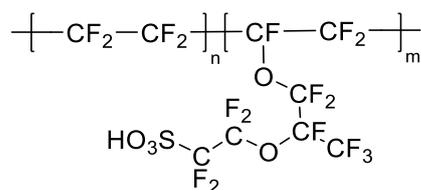

Figure 4. Structure of a Nafion ionomer.

Another approach was provided by Marinescu et al. in 2019. The authors modified different supporting electrode materials with surface-immobilized conjugated polymers by electropolymerization. For this purpose, a [2,2′-bipyridine]5,5′-bis(diazonium) rhenium complex was dissolved in acetonitrile with additional 0.1 M tetrabutylammonium hexafluorophosphate as a conducting salt. Clean electrodes (TiO_2 electrodes) were used as working electrodes. Electrochemical grafting was performed by cyclic voltammetry (CV) in several cycles. An increase in current measured by CV proved successful electropolymerization and an increasing amount of redox-active rhenium-bipyridine species available on the electrode surface. Film thickness grew with the number of CV cycles and, thus, with the number of catalyst-bipyridine species. The resulting orange films of poly(Re(CO)$_3$Cl[2,2′-bipyridine]-5,5′diyl) were characterized by scanning electron microscopy (SEM) and atomic force microscopy (AFM) among other techniques, showing a uniform and smooth film growth across the chosen substrates. Photocatalysis studies of the conjugated polymers on mesoporous TiO_2 substrates were conducted in DMF with TEOA as sacrificial agent. While the pure TiO_2 substrates only generated 0.11 μmol CO in 5 h, the substrate with the lowest amount of conjugated polymer, electropolymerized with using solely one CV scan, showed a TON of 70 and a TOF of 14 h^{-1} after 5 h of irradiation. Using a substrate with higher catalyst loading, produced by five CV cycles, increased the TON to up to 31 with a TOF of 6.1 h^{-1}. Films with even higher catalyst loadings did not exceed these numbers, which indicated that only small quantities of deposited active material remained active over the 5 h of irradiation [47].

2.2. Ni, Fe, Mn-Systems

Cheaper and more abundant non-noble metals were also tested, as their potential for practical applications is greater due to their lower prices, greater availability, and lower toxicities. Very recently, Wang, Wang and Cao used another technique for immobilizing catalysts on semiconductors for an enhanced charge separation. They published a hybrid assembly with Nickel poly-pyridine polymers (NiP) binding on CdS quantum dots (QDs) via thiophene immobilization. NiP was synthesized by polymerizing 2-vinylthiophene and nickel poly-pyridine complex (NIL) mediated by azobisisobutyronitrile (AIBN) [48]. MPA-CdS QDs (MPA = 3-mercaptopropionic acid) were prepared according to another publication [49]. Since NiP contained thiophene units, mixing NiP and MPA-CdS QDs resulted in CdS-Ni assemblies due to the binding affinity between sulfur and cadmium The assembly was investigated by high-resolution TEM (HR-TEM), X-ray photoelectron spectroscopy (XPS), Fourier-transform infrared spectroscopy (FT-IR), and ICP-MS. Photocatalytic activity in terms of CO_2 reduction was tested in a mixture of water and TEOA as the electron donor. The new material assembly provided syngas production with 5500 µmol g^{-1} h^{-1} under visible light irradiation. Syngas is an important feedstock for the chemical industry, consisting primarily of hydrogen and carbon monoxide as it is industrially used, e.g., for Fischer-Tropsch processes. The syngas composition could be controlled upon changing the ratios of MPA-CdS QDs and NiP during the assembly. With a 1:1 ratio of the two material components, the H_2/CO ratio was observed to be around 4:1. The H_2/CO ration was adjustable from 4:1 to 1:3 with lower NiP concentration compared to CdS cores indicating that the nickel center was more sensitive to H_2 production, whereas higher CdS amounts seemed to yield more CO [48].

3. 2D- or 3D-Coordination Networks

3.1. Supramolecular Polymers and Polymer Gels

Another strategy to design photosynthetic systems are self-assembled supramolecular polymers. This class of material opens the possibility for customizable systems with tailored functionalities. Covalently connected polymer gels enable the co-location of, e.g., a photosensitizer and a catalyst, as nature presents in its photosynthesis and energy-conversion devices. The covalent bonding of functional groups for photocatalytic reduction within the artificial supramolecular systems increases the efficiency of electron transfer, leading to an enhancement of chemical transformations [50]. Moreover, certain structures are able to undergo π-stacking. Previous research has shown that π-π stacked supramolecular polymers are accompanied by enhanced charge separation [51]. Stupp et al. specialized in synthesizing self-assembled supramolecular polymers that can feature both: photosensitize CO_2 reduction reactions while remaining stable in aqueous reaction media. Their strategy included using supramolecular polymers containing chromophores for light absorption and a catalyst that can promote CO_2 reduction [52]. Amphiphilic structures are the prerequisite for the self-assembly of tailored structures in an aqueous environment [53]. Therefore, amphiphilic chromophores with diareno-fused ullazine cores were used as monomers. 1,3-dipolar cycloaddition of azomethine ylide with dipolarophile *tert*-butyl 6-maleimidohexanoate was used for the synthesis of compounds 1 and 2 (Figure 5). For generating amphiphilicity, monomers bearing monoimide groups containing carboxylic acids as hydrophilic head group were introduced. *n*-Pentyl tails served as hydrophobic units. The extension of the ullazine core and its π-system by two benzo (1) or two thieno rings (2) improved the absorption ability for visible light, as proven by UV-vis absorption and fluorescence spectroscopy. Aqueous self-assembly was enabled by dissolving the free acids in water using equimolar amounts of NaOH, followed by the addition of NaCl. Self-assembled in water, the monomers built entangled fibers on a nanoscale, as proven by cryogenic transmission electron microscopy (cryo-TEM) resulting in hydrogel formation. The hydrogels were further coupled with a binuclear cobalt catalyst. Photocatalytic CO_2 reduction was first performed in acetonitrile (MeCN) and water mixtures, but also in pure water, while all experiments contained TEOA as a sacrificing electron donor. CH_4

and CO were produced with turnover numbers of $TON_{CO} = 1136$ and $TON_{CH4} = 490$ using the self-assembled cobalt-nanofibers (1) with benzo rings, and $TON_{CO} = 1525$ and $TON_{CH4} = 865$ for the other system, and (2) with thieno rings under blue 450 nm light irradiation for 48 h. The photocatalytic activity of fibers (2) was also shown to be stable over 6 days in a fully aqueous medium with turn over numbers of 4625 and 1518 for CO and CH_4, respectively. Mechanistic studies revealed an oxidative electron transfer from the sacrificing agent TEOA to the sensitizing hydrogel, which donated electrons to the cobalt-active sites for CO_2 reduction, resulting in CO and CH_4 production [52].
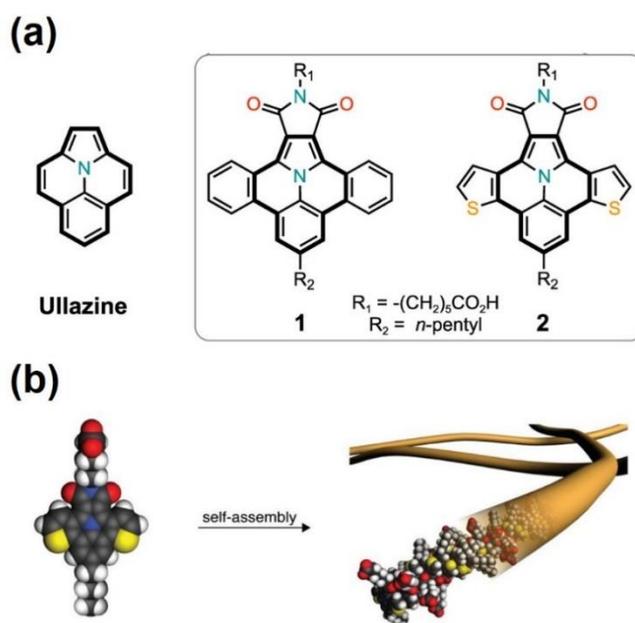

Figure 5. (**a**) Chemical structures of ullazine and diareno-fused ullazines with two benzo (1) and two thieno rings (2); (**b**) Molecular graphics of ullazine (2) and its self-assembly into a supramolecular fiber. Adapted with permission from Ref. [52]. Copyright 2022, American Chemical Society.

Recently, Maji et al. reported on a metal-organic coordination polymer gel as a material for carbon dioxide reduction. As the low molecular weight gelator (LMWG), the authors used a porphyrin core connected to four terpyridine units (TPY-POR). It was synthesized by an amide coupling reaction of 4,4',4'',4'''-(Porphine-5,10,15,20-tetrayl)tetrakis benzoic acid with 2,2':6',2''-terpyridine-4'-yl-propane-1,3-diamine (Figure 6). While the four amide units acted as H-bonding sites, the terpyridine units were used to bind four metal complexes. Moreover, the terpyridine moieties served as the linkers, improving exciton mobility and overall charge mobility. Self-assembly was proven by HR-TEM and powder X-ray diffraction (XRD) studies. The porphyrin-based monomers self-assembled together with Ru(II) ions to a fully coordinated polymer gel (Ru-TPY-POR CPG) (Figure 6a) [54]. Ru(II) was chosen due to its well-studied photocatalytic activity [55]. The self-assembly was promoted by intermolecular π-π stacking and H-bond interaction between the chromophores. The nanoscopic material combined a chromophore acting as a photosensitizer and a catalyst and thus enabled charge transport within the entire network. This novel metal-organic gel showed impressive conversion of CO_2 to CO in the presence of triethylamine (TEA) sacrificial electron donor under visible light irradiation in an acetonitrile/water mixture. A high production rate of 3500 μmol g^{-1} h^{-1} with a selectivity of over 99% over CH_4 was observed when using TEA as SA (Figure 6b). Furthermore, the catalyst was stable without losing its performance for more than six cycles [54]. Previous research showed that the addition of BNAH was beneficial for photoreduction due to lower oxidation potential in comparison to TEA [56]. In this study, the addition of BNAH along with TEA facilitated the formation of CH_4 with a selectivity of 95% over CO, with a high production rate of 6700 μmol g^{-1} h^{-1}. CH_4 was more difficult to produce as it required an $8e^-/8H^+$

reduction process but quenching of BNAH enabled this complex reduction (Figure 6c). All photocatalytic reactions, with and without the addition of BNAH, were also proved to happen equally under natural sunlight irradiation instead with the use of an artificial Xe lamp providing visible light. Mechanistic investigations included in situ diffuse reflectance infrared Fourier-transform spectroscopy measurements and quantum chemical calculations for computing Gibbs free energies. It was revealed that the porphyrin units acted as a photosensitizer and $[Ru(TPY)_2]^{2+}$ as the catalytic centers for CO_2 reduction. The first mechanistic step was the photoexcitation of porphyrin accompanied by one electron transferred to $[Ru(TPY)_2]^{2+}$, resulting in $[Ru^{II}(TPY^{\bullet-})(TPY)]^+$. The intermediate was then reduced to $[Ru^{I}(TPY^{\bullet-})(TPY)]$. One pyridine nitrogen was substituted by CO_2 to form $[Ru^{II}(TPY)(\eta^2\text{-}TPY)(COO^{2-})]$. The next protonation step was shown to be thermodynamically favored resulting in $[Ru^{II}(TPY)(\eta^2\text{-}TPY)(COOH^-)]^+$. Further protonation was accompanied by the elimination of a water molecule to result in $[Ru^{II}(TPY)(\eta^2\text{-}TPY)(CO)]^{2+}$. Reduction and desorption of CO enabled the regeneration of $[Ru^{II}(TPY^{\bullet-})(TPY)]^+$. This regeneration step could not be shown in the presence of BNAH. When BNAH was oxidized, deprotonation and further dimerization to BNA_2 was induced [54]. The reduction potential of the BNA_2 dimer exceeded the one of BNAH, facilitating the quenching of the photosensitizer [56]. $[Ru^{II}(TPY^{\bullet-})(\eta^2\text{-}TPY)(CO)]^+$ was protonated by BNAH to $[Ru^{II}(TPY^{\bullet-})(\eta^2\text{-}TPY)(COH)]^+$. The higher reduction potential of BNAH enabled further reduction and protonation to $[Ru^{II}(TPY^{\bullet-})(\eta^2\text{-}TPY)(CH_2O)]^+$, $[Ru^{II}(TPY^{\bullet-})(\eta^2\text{-}TPY)(OCH_3)]^+$, and $[Ru^{II}(TPY^{\bullet-})(\eta^2\text{-}TPY)(HOCH_3)]^+$. Protonation and simultaneous reduction promoted water elimination to produce $[Ru^{II}(TPY^{\bullet-})(\eta^2\text{-}TPY)(CH_3)]^+$. Final proton-coupled electron transfer released CH_4 and $[Ru^{II}(TPY^{\bullet-})(TPY)]^+$ was regenerated. These mechanistic insights revealed that covalent linkage of the photosensitizer and the catalyst could be a key factor for high performances and the choice of SA is critical for product selectivity [54].
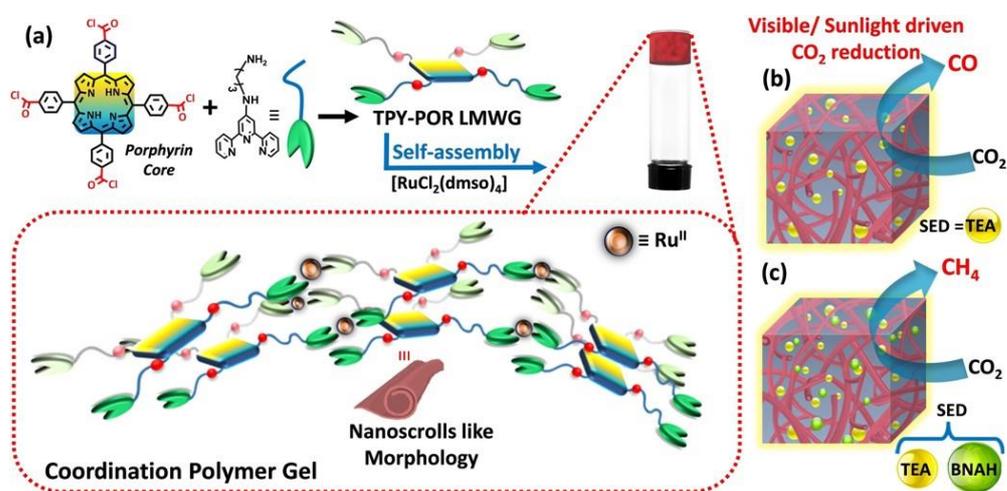

Figure 6. (**a**) Synthesis and self-assembly of TPY-POR LMWG monomers with $[RuCl_2(dmso)_4]$ (dmso = dimethyl sulfoxide) to form a coordination polymer gel; (**b**) Visible or sunlight driven CO_2 reduction with TEA as single electron donor (SED); (**c**) Visible or sunlight driven CO_2 reduction with TEA and BNAH as SED. Reprinted with permission from Ref. [54]. Copyright 2022, Wiley-VCH.

In 2020, Sun et al. presented the first pyridyl-salen-based ligands (H_2L) with metal-containing (Mn(III) or Fe(III)) coordination polymers (CPs) that can build supramolecular structures with hydrogen bonds. The ligand combined a pyridine moiety with salen ligands containing N_2O_2 coordination pockets [57]. Pyridine moieties are known to be stable catalysts for aqueous electrochemical reductions in multiple-electrons and multiple-protons [58–60] but lack light absorption. Salen moieties have attractive light absorption properties and electron transfer ability together with the CPs. No matter which metal center was used (Mn(III) or Fe(III)), the coordination polymers showed high photocatalytic

activity, as measured by electrochemical impedance spectroscopy (EIS). Nevertheless, Fe(III) materials had a slightly faster interfacial charge transfer and, thus, a better performance than Mn(III). EPR studies helped to unravel the reaction mechanism of the pyridyl-salen coordination polymer system paired with TEOA hydrogen and electron donor. These results implied that the ligand center acted as the catalytic active site and not the Fe(III)/Mn(III) metal center in the reduction from CO_2 to CO. CO was observed as the only product in the gas phase. It was produced by the Fe(III) CP with 31.6 μmol g^{-1} h^{-1}, by Mn(III) CP with 14.3 μmol g^{-1} h^{-1}, and by the single ligand with 4 μmol g^{-1} h^{-1}. After light absorption and reduction by TEOA, the ligand radical of H_2L was formed, reducing CO_2. The superior catalytic activity of the porous organic polymer together with Fe(III) coordination could be explained by improved light absorption, as well as the enhanced separation of charge carriers [57].

Recently published in 2022, Mellot-Draznieks and Dolbecq revealed insights into the mechanism of photocatalytic CO_2 reduction via density functional theory (DFT) calculations. Therefore, the groups synthesized three heterometallic molybdenum(V) phosphates containing polyoxometalate (POM) units under hydrothermal conditions. A metal ion of either Mn(II) or Co(II) was embedded between two $P_4Mo_6{}^V$ anionic rings. For the generation of a completely inorganic photocatalyst, Fe(II) ions were mixed with the Mn(II)-containing reaction medium building a 3D network of Fe-Mn. Fe(II) and Fe(III) as well as Mn(II) centers connect the POM units in a network acting as counter ions to extra phosphate ions, that do not belong to P_4Mo_6 rings (Figure 7a). Besides the latter novel structure, additional structures were synthesized by $[Ru(bpy)_3]^{2+}$ complexes that were added to both Mn(II) and Co(II) POM unit solutions. The Ru bipyridine complexes served as counter ions to the anionic chains that were connected via Mn(II) and Co(II) ions to Ru(bpy)-Mn and Ru(bpy)-Co hybrids. Testing all three compounds for photoreduction, solely Fe-Mn and Ru(bpy)-Mn complexes were able to catalyze the reduction of CO_2 to CH_4 and CO as a side product. TEOA was used as a sacrificing agent and $[Ru(bpy)_3]^{2+}$ as a photosensitizer. DFT calculations of these bipyridine systems revealed new knowledge leading to a novel proposed mechanism, in which $[Ru(bpy)_3]^{2+}$ acted as a catalyst and the POM material as a co-catalyst (Figure 7b). The $[Ru(bpy)_3]^{2+}$ complex was reduced via photoionization in a one-electron process to yield the $[Ru^{II}(bpy)_2(bpy^{\bullet-})]^+$. One-electron charge transfer to the solvent (water) reconverted this structure to a $[Ru(bpy)_3]^{2+}$ species. The electron was solvated and could reduce CO_2 to $CO_2{}^{\bullet-}$ because of its tendency to localize in an empty π^* molecular orbital of the carbon dioxide. The reduced $CO_2{}^{\bullet-}$ coordinated to a metal(II) ion (e.g., Mn(II)) via its carbon atom by replacing a water ligand that was coordinated to the metal atom, forming a metal-COO$^{\bullet-}$ intermediate. This Mn-COO$^{\bullet-}$ intermediate was further reacted to Mn-COOH via electron transfer from a POM cluster and proton transfer from HTEOA$^+$. At this point, reduced POM units, acting as a co-catalyst, and the sacrificing agent, which can generate protons via photooxidation, were both involved. Another suggestion was made that TEOA$^\bullet$ might act as a proton and electron donor concurrently. For C-O(H) cleavage, Mn-COOH was again protonated by a second HTEOA$^+$. The author showed the necessity of a metal-containing photosystem because otherwise $CO_2{}^{\bullet-}$ itself would dimerize to oxalate. Further suggestions were made that CO could probably be reduced to CH_4 by the POM materials and TEOA without the influence of $[Ru(bpy)_3]^{2+}$. For the system containing Co(II)-POM units and $[Ru(bpy)_3]^{2+}$, DFT calculations could additionally show that these systems were unable to reduce CO_2. The authors stated that Co(II) units dimerized while adsorbing an additional electron, making them inactive for CO_2 reduction [61].

3.2. Porous Organic Polymers

Porous organic polymers (POPs) are macromolecules mainly composed of carbon, nitrogen, and oxygen atoms, in addition to other non-metallic chemical elements that are linked covalently. POPs possess high porosity with permanent pores due to their tailor-made structures. They can be classified by crystallinity to distinguish between crystalline

covariant organic frameworks (COFs) and amorphous polymers. Amorphous polymers contain a wide variety of materials such as conjugated microporous polymers (CMPs), hyper-crosslinked polymers (HCPs), etc. [62]. Covalent triazine frameworks (CTFs) are another class of POPs that, based on current research, contain crystalline and amorphous materials. Their aromatic CN-linkage of the triazine unit, as well as the absence of weak bonds, gives them unique characteristics [63]. The porous structure makes the substrate accessible for small gas molecules and thus provides enhanced gas adsorption ability.
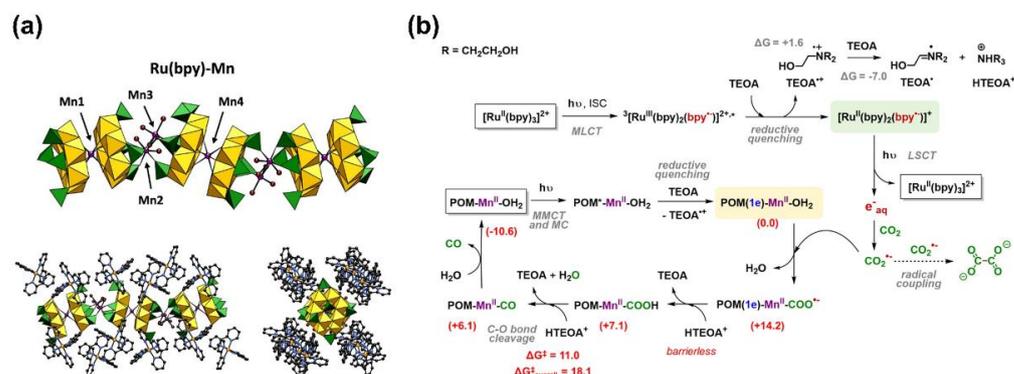

Figure 7. (**a**) Generation of chains by connected $M(P_4Mo_6)$ sandwich-type POMs with Mn(II) ions, side (left) and top view (right); (**b**) Schematic presentation of the mechanism of the photocatalytic reduction of CO_2 to CO with $[Ru(bpy)_3]^{2+}$ as a photosensitizer and TEOA as sacrificial agent using a POM system bearing Mn(II). Gibbs free energies (ΔG) are given in kcal mol^{-1}. MLCT, ISC, MMCT, MC, and LSCT are abbreviations for metal-to-ligand charge transfer, intersystem crossing, metal-to-metal charge transfer, metal-centered, and ligand-to-solvent charge transfer, respectively. Adapted with permission from Ref. [61]. Copyright 2021, American Chemical Society.

POPs in general are a class of versatile materials due to their broad light absorption range caused by the tunable positions of both: the valence and conduction band. They offer even more tunable characteristics such as surface area or the incorporation of different functionalities by adding various building blocks or active sites. The surface area is characterized by the Brunner-Emmet-Teller (BET) specific surface area. Besides the surface area, pore sizes as well as chemical structure are variable to tune the CO_2 adsorption capability [62,64].

Thornton et al. introduced four general steps for the catalytic process of CO_2 reduction with zeolite catalysts [65]. Zeolites are aluminosilicates in which the crystalline 3D structure is built from four-connected tetrahedral frameworks making them microporous minerals [66]. The zeolites' photocatalytic mechanism can be adapted to POPs: (1) Carbon dioxide diffuses into the active sites of the material, (2) CO_2 is adsorbed on the active catalytic sites, (3) carbon dioxide is converted into product species, and (4) the product molecules are desorbed and leave the material [65].

3.2.1. Crystalline Frameworks

COFs offer an extended π-system due to the covalent organic framework and the supplementary crystallinity. The high conjugation degree enhances the transport and separation of photogenerated electrons and holes, which boosts charge separation for enhancing the lifespan of excited states [67].

Noble metals, such as Re or Ru, have shown to be suitable components for photocatalytic CO_2 conversion, especially when mixed with organic networks. The groups of Thomas and Han used $FeCl_3$-promoted oxidative coupling polymerization of 5,5'-di(9*H*-carbazol-9-yl)-2,2'-bipyridine (CM1) or 3,8-di(9*H*-carbazol-9-yl)-1,10-phenanthroline (CM2) to produce porous polycarbazole networks and included catalytic rhenium(II) centers in their materials (Figure 8). The authors compared two materials: a bipyridine-based (CPOP-30) and a phenanthroline-based (CPOP-31) polycarbazole network. Both materi-

als contained nitrogen-units for anchoring Re(I) active species, so that the polycarbazole networks could be metalated to CPOP-30-Re/CPOP-31-Re via the post-synthetic route by metalation of the polycarbazole. Direct polymerization of carbazole-rhenium monomers resulted in CPOP-30′-Re. All carbazole networks, CPOP-30-Re, CPOP-30′-Re and CPOP-31-Re, formed covalent organic frameworks (COFs) with a regular π-π stacked structure. The metal-loaded polymer networks were used as photocatalysts in organic solvents, with an additional sacrificial agent TEOA or TEA. CPOP-30′-Re lacked in performance as it only had a CO production of 3.2 3 μmol within four hours and 10 mg of catalyst. The pyridine-based COF CPOP-30-Re outperformed the phenanthroline-based CPOP-31-Re framework. The phenanthroline framework had a larger delocalization of charges and less negative reduction potential, weakening the thermodynamic driving forces and thus the performance in CO_2 reduction. The authors found out that the frameworks themselves also performed as light-harvesting photosensitizers besides keeping chelating sites. With the pyridine-based framework, CO formation could be achieved with production rates up to 623 μmol g^{-1} h^{-1} in less than 10 h with a CO selectivity of almost 98% [68].
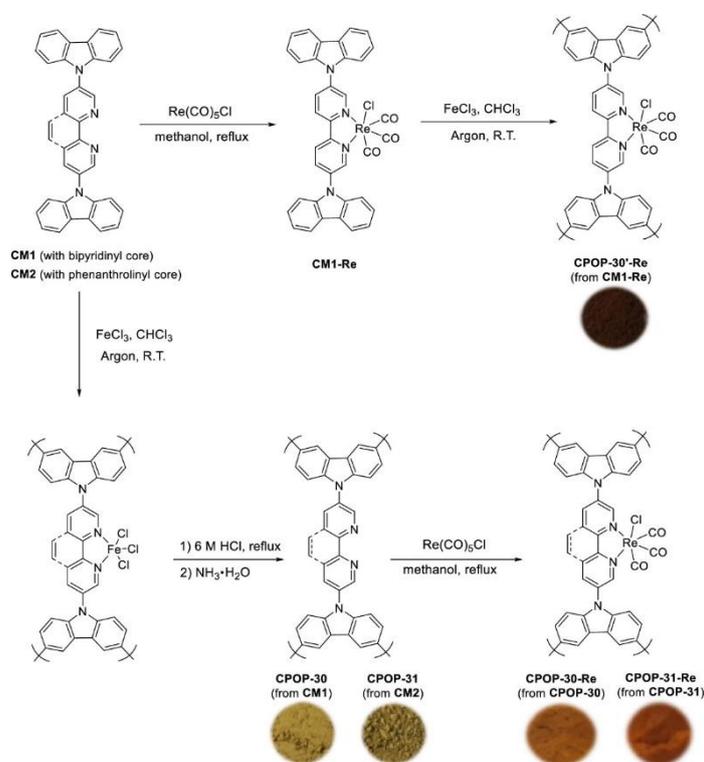

Figure 8. Direct polymerization of carbazole-based, rhenium-bearing monomers resulting in CPOP-30′-Re and synthesis of rhenium-metalated polypyridine-based porous polycarbazole networks (CPOPs) via post-synthetic metalation of CPOP-30 or CPOP-31. Reprinted with permission from Ref. [68]. Copyright 2019, American Chemical Society.

In a similar approach, Chen, Sprick, and Cooper used bipyridine units in an oligomer-linked framework for anchoring Re(I) complexes. The authors utilized Knoevenagel condensation reactions of 1,3,6,8-tetrakis(4-formylphenyl)pyrene (TFPPy) and 5,5′-bis(cyanomethyl)-2,20-bipyridine to obtain a fully π-conjugated backbone and thus an increased conjugation framework. Besides bipyridine for anchoring [Re(CO)₅Cl] complexes via post-synthetic modification, the COF comprised cyanovinyl-groups due to the Knoevenagel reaction, which supported CO_2 uptake. Transient absorption spectra revealed a long-lived charge separated state by the presence of Re within the COF. Computational calculations including DFT and time-dependent (TD) DFT calculations proved electron transfer upon electronic excitation from the COF backbone to the anchored Re-complexes. Photocatalytic reduction experiments were performed under visible light in acetonitrile, with TEOA as a sacrificial

agent. CO production showed a selectivity of 81% and a rate of up to 1040 μmol g^{-1} h^{-1}. With the addition of a supplementary photosensitizer 4,4′-*bis*(1,1-dimethylethyl)-2,2′-bipyridine-*N*1,*N*1′]*bis*[3,5-difluoro-2-[5-(trifluoromethyl)-2-pyridinyl-*N*]phenyl-C]iridium(III)-hexa-fluorophosphate (Ir[dF(CF$_3$)ppy]$_2$(dtbpy))PF$_6$ (dF = difluoro, ppy = 2-phenylpyridine, dtbpy = 4,4′-di-tert-butyl-2,2′-dipyridyl)), embedded in the accessible pores of the COF, the CO production rate was maximized to 1400 μmol g^{-1} h^{-1} and a selectivity of 86% was reached by an electron transfer mechanism between the photosensitizer and COF by oxidative quenching. Moreover, colloidal Pt was added via in situ photodeposition. The formation of syngas was enhanced and the H_2:CO ratio was influenced from 1:4 to up to 10:1 by adding different amounts of Pt between 0 and 4 wt.%. Higher amounts of Pt caused higher selectivity towards H_2 [69].

Zhang and Huang designed a 2D-COF consisting of 2,2-bipyridyl-5,5-dialdehyde (BPDA) and 4,4′,4″-(1,3,5-triazine-2,4,6-triyl)trianiline (TTA) reacted via solvothermal reactions (Figure 9a). Postsynthetic incorporation of [Re(CO)$_5$Cl] formed Re-COF systems. Single COFs stacked together in an AA stacking mode (Figure 9b,c) so that all layers showed identical lateral coordinates. These observations were supported by simulations using Material Studio 8.0 since this stacking was calculated to be the most probable state. In situ diffuse reflectance UV-vis spectroscopy helped to reveal mechanistic details (Figure 9d). Absorption of light induced an intramolecular charge transfer by the Re-COF structure, which was immediately quenched by TEOA, resulting in a TEOA$^+$-(COF-Re)$^-$ state with charge separation. Afterwards, CO_2-Re complexes were formed after Cl$^-$ dissociated from the Re precursor. Finally, CO was steadily generated, which was assigned as the rate limiting step of the reaction [70].
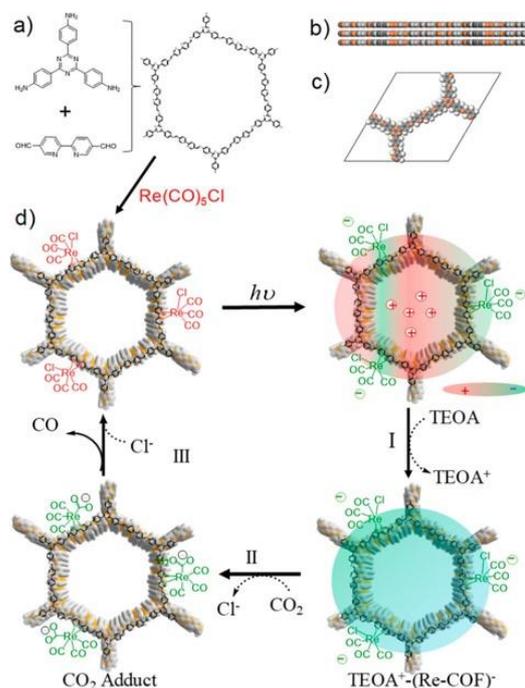

Figure 9. (**a**) Synthesis approach of the 2D COF; (**b**) Side view of AA stacking; (**c**) Unit cell of AA stacking COF; (**d**) Proposed mechanism of the photocatalytic CO_2 reduction. Reprinted with permission from Ref. [70]. Copyright 2019, American Chemical Society.

A novel approach in the field of photocatalysts for CO_2 reduction was reported in 2017 by Inagaki and Ishida et al. They were the first to use periodic mesoporous organosilica (PMO) containing bipyridyl ligands in the pore walls. These bipyridyl units facilitated the coordination of two different metal complexes: a Ru photosensitizer (Ru(PS)) and a Ru catalyst (Ru(Cat)) by stepwise reaction to build a heterogeneous photocatalyst structure with the active sites being embedded inside the pores. Photochemical reduction in CO_2

under visible light with the Ru(PS)-Ru(Cat)-Bpy-PMO system in aqueous dimethylamine (DMA) solution and BNAH as electron donor yielded CO and formate as products. Molar fractions of the photosensitizer and catalyst (*x*, *y*) were determined by XRD measurements. Moreover, the molar fraction of Ru(Cat) (*y*) was also quantified by the amounts of CO being dissociated from the Ru(Cat) under UV-light irradiation. The (*x*, *y*) ratio could influence the product selectivity. The CO selectivity increased by raising molar fractions of Ru(PS) to $x = 0.11$ and Ru(Cat) to $y = 0.055$, resulting in TONs over $162 \, h^{-1}$ and a CO selectivity of 47% vs. 37% for formate. The durability of the tested POMs was sufficient to be recycled and reused at least three times [71].

Cheaper and more abundant non-noble metals were also tested as photocatalysts in COF structures. In 2019, Lan et al. reported on COF structures built from covalently linked 5,10,15,20-tetrakis(4-aminophenyl)-porphinato (TAPP-M, M = 2H, Zn, Ni, Cu) and 2,3,6,7-tetra(4-formylphenyl)-tetrathiafulvalene by Schiff-base condensation resulting in (TTCOF-M). Testing CO_2 reduction without using any sacrificial agent or co-catalyst, only TTCOF-Cu and TTCOF-Zn, showed significant photocatalytic activity. TTCOF-Zn showed the highest CO production, with values of 12.33 μmol after 60 h; TTCOF-Cu performed weaker and caused a CO production of 8.65 μmol. The authors proposed an intrinsic mechanism for their COFs with metalloporphyrin and tetrathiafulvalene moieties. After photoexcitation, the tetrathiafulvalene moieties functioning as HOMO centers transferred the electrons to the metalloporphyrins serving as LUMO centers. Afterwards, the electrons were transported to the catalytic metal centers in the TAPP units for CO_2 reduction, while H_2O was oxidized by tetrathiafulvalene gaining electrons for charge balance. No photosensitizer, sacrificial agents or co-catalyst were needed for a CO selectivity of almost 100% [72].

Wang et al. designed porphyrin-tetraphenylethene-based COFs (MP-TPE-COF) with anchored Ni(II) metals. The anchored Nickel caused a CO production rate of $525 \, \mu mol \, g^{-1} \, h^{-1}$ with 93% selectivity, as well as a high durability in aqueous solution. TEOA served as an electron donor and $[Ru(bpy)_3]Cl_2$ as a photosensitizer. Besides DFT calculations, mechanistic investigations included EIS and steady-state photoluminescence measurements: the photosensitizer was excited and reduced Ni(II) to give Ni^0 which could adsorb and activate CO_2. Protonation generated coordinated COOH species to the Ni(II) intermediate. Protonation and water release produced CO as a product and regenerated Ni(II) active sites [73].

$2,2'$-bipyridine-based COFs with single Ni sites were reported by Yu and Zou in 2019. Condensation of 1,3,5-triformylphloroglucinol and $5,5'$-diamino-$2,2'$-bipyridine under solvothermal conditions led to the $2,2'$-bipyridine-based COF (TpBpy). Treatment of TpBpy with $Ni(ClO_4)_2$ inserted Ni ions to give Ni-TpBpy. FT-IR spectroscopy and ^{13}C-NMR spectroscopy revealed the preservation of the COF structure after Ni loading and XPS measurements confirmed the successful Nickel loading. N_2 adsorption and desorption measurements showed a decrease in the BET surface area from 973 to $580 \, m^2 \, g^{-1}$, which further indicated the loading with Ni(II) ions in the COF structure by chelation of the bipyridine binding units. The photocatalytic activity in CO_2 reduction was measured in aqueous acetonitrile, with TEOA as a sacrificing agent and a Ru photosensitizer. The system induced a CO production rate of $811 \, \mu mol \, g^{-1} \, h^{-1}$ with a selectivity of 96%. The experimental data and DFT calculations opened suggestions for a mechanism: the $[Ru(bpy)_3]^{2+}$ photosensitizer was first excited. Then, the excited electrons were transferred through the COF to the adsorbed CO_2 on the Ni(II) sites. Higher CO_2 affinity of the Ni sites in comparison to H^+ adsorption determined the selectivity of the formed product in terms of inhibiting H_2 formation. Compared to free CO_2, adsorbed species had a bended configuration demonstrating its activation by metal sites (Figure 10). In general, the bipyridine moiety hosted the CO_2 and metallic catalytic centers and additionally facilitated the activation of CO_2. This combined functionality could be enabled by synergistic effects between the catalytic sites and the framework [74].
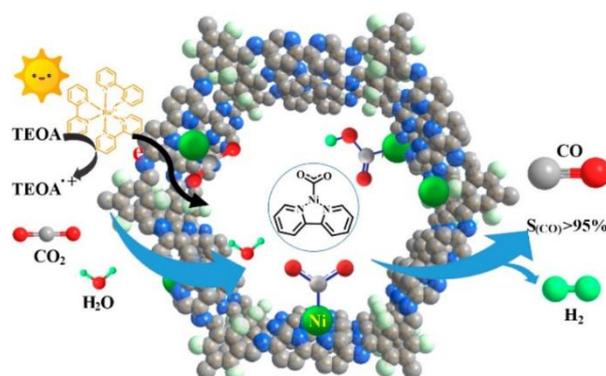
Figure 10. Schematic diagram of the photocatalytic CO_2 reduction by a 2,2′-bipyridine-based COF with embedded Nickel sites. Reprinted with permission from Ref. [74]. Copyright 2019, American Chemical Society.

Further networks such as porous polycarbazoles or porous covalent triazine frameworks were investigated as materials to support photocatalytic carbon dioxide reduction. Just recently in 2022, Byun and Wang published their work on crystalline porous organic polymers (CPOPs) consisting of polycarbazoles functionalized with various transition-metal complexes. The CPOPs were synthesized by simple one-pot oxidative coupling polymerization by using 1,3,5-tri(9H-carbazol-9-yl)benzene as a precursor, promoted by $FeCl_3$. CPOPs themselves, showed a capacity to capture CO_2 due to their microporosity and a high surface area. After synthesis, the obtained CPOPs were dispersed in chloroform and mixed with either iron chloride, cobalt chloride, or nickel chloride for metal impregnation to give CPOP-Fe, CPOP-Co, and CPOP-Ni, respectively. The metal species were anchored within the porous network, as proven by scanning electron microscopy, FT-IR, powder-XRD, N_2 physisorption, and diffuse reflectance (DR) measurements. The unpaired electrons in the 3d-orbitals of the transition metal centers were delocalized and were able to react with anti-bonding π-orbitals of CO_2. Photocatalytic activity was tested in aqueous acetonitrile solution under visible light irradiation with $[Ru(bpy)_3]^{2+}$ as a photosensitizer and TEOA as a sacrificial agent. The mechanism for a Ni-loaded CPOP was proposed as follows: PS^{2+} was excited by light absorption and PS^{2+*} was formed. TEOA reduced this state to give PS^+. The excited electron was transferred to the Ni active site at which CO_2 was coordinated to the metal. Activation of the C=O double bond led to negatively charged CO_2^-. The electron was transferred to the adsorbed CO_2 and formed a CO_2^* intermediate. After further protonation and reduction, H_2O and CO were released (Figure 11). Different metal ions had an impact on the kinetics of activation and, consequently, product selectivity and production rate. The CPOP-Co showed the best results, with a CO production rate of 31,000 μmol g^{-1} h^{-1}; however, this just led to a CO selectivity of 55%. While CPOP-Ni produced CO with a production rate of 28,000 μmol g^{-1} h^{-1} with 89% selectivity, CPOP-Fe lacked in both production rate and selectivity compared to the other two transition metals [75].

Huang and Cao were the first to use porous covalent triazine frameworks (CTFs), modified with a rhenium-based catalyst, for photocatalytic CO_2 conversion [76]. CTFs had already been known as gas adsorption materials due to their porous structure [76–78]. The CTF structure was based on 2,6-dicyanopyridin (CTF-py), so that the nitrogen units provided the possibility to act as anchor sites for metal catalyst molecules. A $[Re(CO)_5Cl]$ complex, which can act as both photosensitizer and photocatalyst, was coordinated to these nitrogen sites via ionic thermal synthesis to give Re-CTF-py networks. In a gas–solid system including TEOA as a sacrificing agent, CO was produced with a rate of up to 353 μmol g^{-1} h^{-1} and a TON of 4.8 within 10 h. In this solid-gas system, the photocatalyst was not dissolved in a solution, instead the Re-CTF-py was dispersed on a quartz film and

a MeCN/water mixture was added to the cell. Leaching of the active Re sites was prevented and the catalyst showed better recyclability [76].
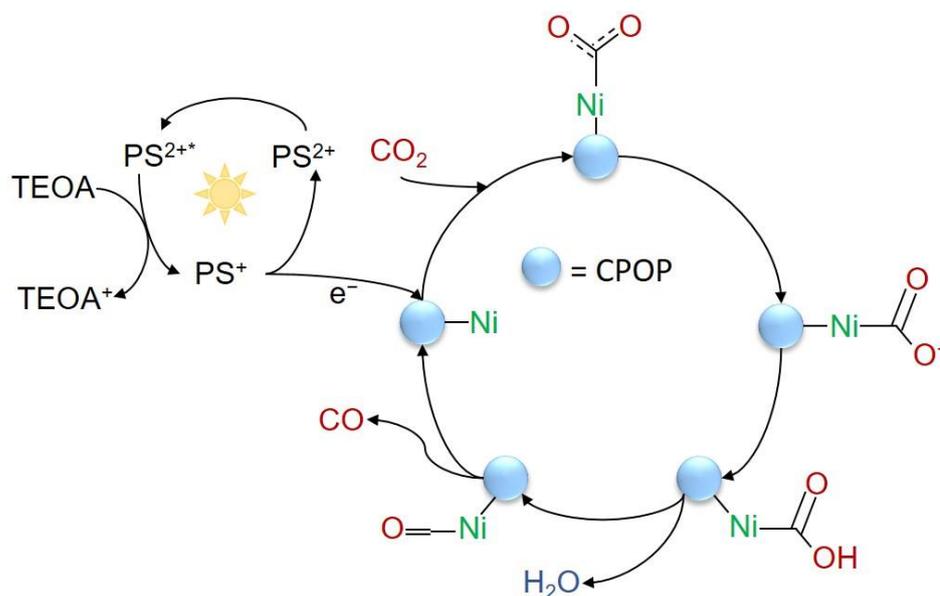

Figure 11. Proposed mechanism for the photocatalytic CO_2 reduction by a Ni-loaded CPOP. Data from Ref. [75].

Wang, Zeng, and Jiang opened the path for a scalable bottom-up synthesis of two-dimensional (2D) COF nanosheets. The synthesis approach included an imine-exchange strategy. 5,10,15,20-tetra(*p*-aminophenyl)porphyrin (H_2TAPP) reacted with 4, 4′-biphenyldialdehyde (BPDA) under solvothermal conditions. Afterwards, the addition of an excess amount of 2,4,6-trimethylbenzaldehyde (TBA) enabled the 2D imine-linkage to give COF-367 nanosheets (NSs) (Figure 12). TBA prevented π-π stacking of the single COF nanosheets due to methyl side groups, enabling anisotropic growth along the planar nanosheet direction. Using CoTAPP instead of H_2TAPP resulted in Co(II) porphyrin (CoPor)-based COF-367-Co NSs. As a proof-of-concept, the photocatalytic performance of the COF-367-Co NSs was explored under visible light irradiation. In an 0.1 M $KHCO_3$ aqueous solution with [Ru(bpy)$_3$]$^{2+}$ photosensitizer and ascorbic acid (AA) as the sacrificial agent and electron donor, the production rate of CO from CO_2 was remarkably high, with a value of 10,162 μmol g^{-1} h^{-1} and a CO selectivity of 78% in comparison to H_2. The whole COF-367-Co catalytic system remained almost stable with a production rate of still 10,000 μmol g^{-1} h^{-1} after six successive cycles. The bulk material, not having a 2D-layered structure, exhibited a CO production rate of only 124 μmol g^{-1} h^{-1}. Mechanistic investigations were performed using photoluminescence and ultrafast transient absorption spectroscopic experiments. These experiments revealed that [Ru(bpy)$_3$]$^{2+}$ became excited, while AA sacrificed one electron to the Ru to achieve [Ru(bpy)$_3$]$^+$. This electron was further transferred from the Ru complex to the COF. Within the COF, CO_2 was coordinated to the Co(II) atoms. With the electron transfer, COOH* was formed as the coordinated intermediate species. This formation turned out to be the reaction limiting step. DFT calculations revealed a small energy barrier of 0.47 eV for the intermediate formation process. The small energy barrier facilitated the process to occur at room temperature. These insights uncovered that the 2D nanosheet structure enhanced the photocatalytic performance because of its large aspect-ratio. The 2D morphology caused a large number of active sites for a high adsorption capacity on the surface. Compared to the respective bulk material, in which the active sites are rather hidden inside the bulk, the accessibility of active sites on the surface of the nanosheets increased the rate of CO_2 reduction [79].
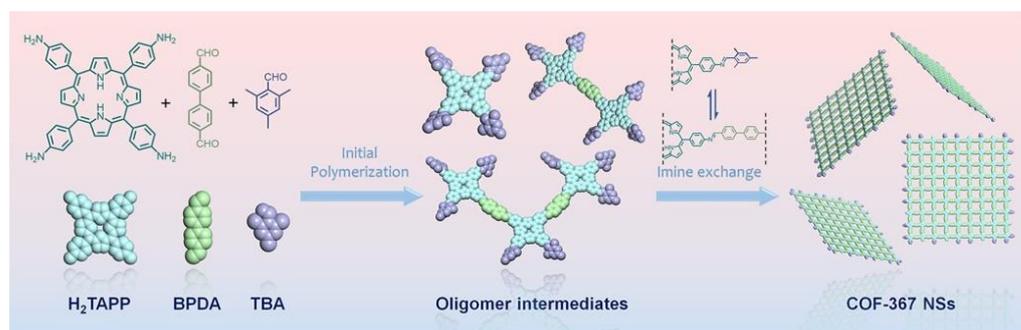
Figure 12. Schematic illustration of the synthesis of COF-367 nanosheets (NSs) via an imine-exchange strategy. Using CoTAPP instead of H_2TAPP led to CoPor based COF-367-Co NSs. Reprinted with permission from Ref. [79]. Copyright 2019, American Chemical Society.

3.2.2. Amorphous POPs

In 2019, Tan et al. stated that high CO_2 conversions needed both efficient photocatalysis with high CO_2 uptakes and short diffusion paths. Therefore, they reported on a novel material which consisted of a porous hyper-crosslinked polymer on TiO_2 functionalized graphene (HCP-TiO_2-FG). TiO_2 is a low cost photocatalyst, HCPs provided a porous network. By the linkage, the advantages of all materials were combined. The material was synthesized by a synthetic strategy which included in situ knitting [80]. First, the functionalized TiO_2-Graphene (TiO_2-FG) was manufactured from TiO_2-graphene (TiO_2-G) by a solvothermal process and the hydroxyl groups on the TiO_2 surface were converted to phenyl groups [81]. The polymer layer was hyper-crosslinked on this TiO_2-FG skeletal structure. Polymer layers were hyper-crosslinked on the TiO_2-FG by knitting of the phenyl groups and 1,3,5-Triphenylbenzene (*syn*-PhPh$_3$), resulting in HCP-TiO_2 [82]. Due to the porosity, a high surface area of 988 $m^2 g^{-1}$ and a CO_2 uptake efficiency of 12.87 wt.% were measured. Without the use of sacrificial agents or a co-catalyst, CH_4 production via a multi-electron process in a gaseous set-up reached a value of 27.63 μmol g^{-1} h^{-1} and a CH_4 selectivity of 83.7% was measured. Methane is a higher valued product than CO as CH_4 can be used as a raw product to be transformed into more complex organic molecules. The composite structure enables a high CO_2 uptake in its pores, as well as short diffusion paths between adsorption and catalysis. Moreover, the HCP absorbed light in a broad range and the graphene layer improved charge separation due to fast charge mobilities [80]. In a similar approach, the same group used HCPs grafted onto a TiO_2 surface metalized with Pd (HCP-TiO_2-Pd). Pd nanoparticles could capture photogenerated electrons and worked as an electron trap. This approach improved the charge separation for the complete reduction reaction. The HCPs were synthesized by copolymerizing N-heterocyclic carbenes (NHC) and benzene. The HCP contained N-heteroatom sites. These were induced defects acting as anchor points for Pd nanoparticles which performed as a co-catalyst. Friedel-Crafts reaction was used to link the phenyl groups of the TiO_2 surface with the HCP network. Because the heteroatom-induced defects of the HCP were spread over the whole material, the Pd sites were distributed evenly (Figure 13). Extensive morphology investigation including high-angle annular dark-field (HAADF) and energy-dispersive spectroscopy (EDS) mapping images proved the covalent linkages, building of a porous HCP network and uniform dispersion of active sites. The photocatalytic performance was tested in a gas–solid reaction system under visible light irradiation, but without the addition of further sacrificial agents or photosensitizers. HCP-TiO_2-Pd showed a production rate of CH_4 of 237 μmol g^{-1} h^{-1} and a selectivity of more than 99.9%. Structural stability was also given; the production rate was maintained with a value of over 80%, even after five cycles. Pd favored subsequent hydrogenation reduction in CO_2, enabling methane formation with a high selectivity [83].

Wang and Zang integrated catalysts to POPs with two different environments, which were metallophthalocyanine and salphen moieties [84]. Metallophthalocyanine POPs

with M-N$_4$ (M = Co, Ni, Cu or Fe) sites are already widely known as active materials for electro- and photocatalysis of CO$_2$ [73,85,86]. Besides the M-N$_4$ metallophthalocyanine environment with M = Ni, salphen M-N$_2$O$_2$ (M = Ni, Co) moieties were integrated in the materials as a second environment. The material was synthesized by polycondensation reaction of nickel(II)-2,3,9,10,16,17,23,24-octakis(amino)phthalocyanine ((NH$_2$)$_8$NiPc) with 2,6-diformylphenol (DFP) in a dimethylacetamide/mesitylene mixture and with the regulating agent aniline. This step was followed by treatment with Ni(OAc)$_2$ × 4 H$_2$O or Co(OAc)$_2$ × 4 H$_2$O, resulting in a porous framework with atomically isolated Ni-N$_4$ and M-N$_2$O$_2$ (M = Ni, Co) sites (Figure 14), denoted as NiPc-NiPOP or NiPc-CoPOP (Figure 14). FT-IR spectroscopy, XPS, Fourier transformed extended X-ray absorption fine structure (FT-EXAFS) spectroscopy, high-angle annular dark-field scanning transmission electron microscopy (HAADF-STEM) and EDS mapping revealed an amorphous structure of the samples and confirmed that one metal ion was incorporated in each of the salphen pockets. The BET surface area was determined to be 333 m^2 g^{-1}. Nonlocal density functional theory (NLDFT) proved the mesoporous character and the accessibility of the catalytic sites. Photocatalytic experiments were conducted under visible light in acetonitrile/water solution with additional [Ru(bpy)$_3$]$^{2+}$ photosensitizer and TEOA sacrificial agent and monitored by gas chromatography. The NiPc-NiPOP material had an extraordinary CO generation of 7.77 mmol g^{-1} with a CO selectivity of 96% after four hours of reaction time and performed better than NiPc-CoPOP. Control experiments and theoretical DFT studies showed that the salphen Ni-N$_2$O$_2$ units were more active for CO$_2$ reduction than the metallophthalocyanine sites [84].
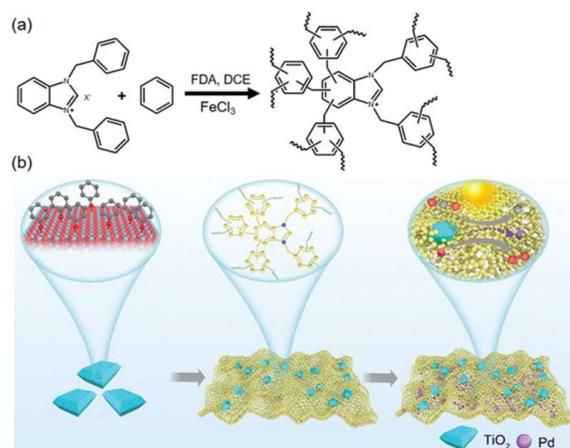

Figure 13. (**a**) Synthesis of NHC-containing HCPs; (**b**) Scheme of the in situ knitting strategy to form HCP-TiO$_2$-Pd. Reprinted with permission from Ref. [83]. Copyright 2021, Wiley-VCH.
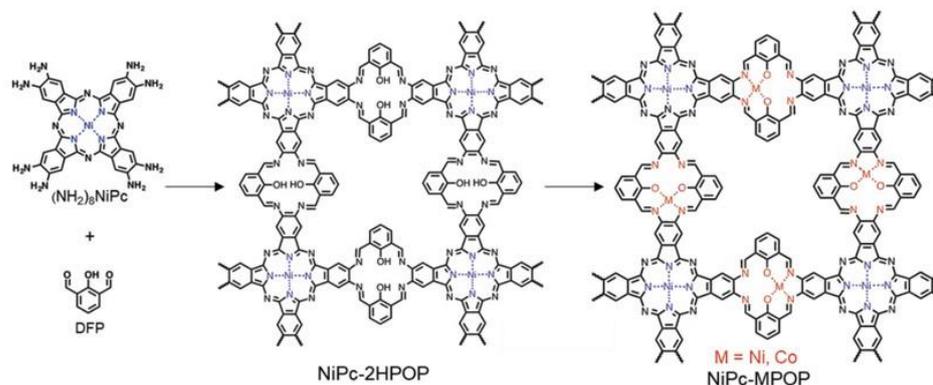

Figure 14. Scheme of the stepwise synthesis of NiPc-MPOP (M = Ni or Co). Reprinted with permission from Ref. [84]. Copyright 2021, Wiley-VCH.

3.3. Metal-Organic Frameworks

Metal–organic frameworks (MOFs) are hybrid crystalline materials, also known as porous coordination polymers (PCPs) or porous coordination networks (PCNs) [87]. They are built by metal ions or metal clusters, serving as nodal points, that are coordinatively linked by organic ligands [88]. The combination of different metals and organic linkers opens the path to millions of distinct MOFs, i.e., over 500,000 have been predicted and 90,000 synthesized so far [89]. Therefore, the number of MOFs reported regarding CO_2 reduction studies is also enormously high. We recommend comprehensive reviews [90,91] on MOFs for carbon dioxide photocatalytic reduction.

MOFs can build 1D, 2D and 3D structures. Among the structural diversity, the main MOF systems that have been investigated so far are zeolitic imidazolate frameworks (ZIFs), carboxylate MOFs, and zirconium-based MOFs [92]. The properties of a MOF are determined by the network connectivity of the single molecules. MOFs have a large internal surface area, and their pores have controllable sizes which have adsorptive sites for capturing gas molecules [14,93]. Tailored MOFs offer the opportunity of incorporating functional species, e.g., in the form of nanoparticles, within the frameworks, which can be prepared within the cavities or be directly encapsulated in the MOFs [94]. Tunable pore sizes as well as surface areas and chemical composition make MOFs versatile materials for photocatalytic CO_2 conversion [95,96]. In a MOF, the metal clusters can serve as reductive sites for CO_2 reduction, while the organic linkers enhance CO_2 adsorption and charge transport [87,91].

In 2014, Luo et al. used iridium as an active light-harvesting agent due to its broad light absorption range and the longevity of its excited states. Ir(III) was embedded into a bi-functional iridium-yttrium coordination polymer photocatalyst of $Y[Ir(ppy)_2(dcbpy)]_2[OH]$ (ppy = 2-phenylpyridine, dcbpy = 2,2′-bipyridine-4,4′-dicarboxylate). The generated complex acted as a photosensitizer for harvesting visible light and, at the same time, as a catalyst for CO_2 reduction. The $[Y(OH)_2(CO_2)_2]∞$ chains were constructed by Y^{3+} ions acting as multi-coordination centers bridged by two OH^- units and two carboxylate groups. This coordination enhanced the stability to construct a 3D supramolecular framework. CO_2 was reduced to $HCOO^-$ in a mixture of MeCN and TEOA with a TOF of 119 $\mu mol\ g^{-1}\ h^{-1}$. The authors proposed a mechanism for MOF-stabilized photocatalyst-mediated CO_2 reduction as follows. After the catalyst was excited by visible light irradiation, TEOA reduced this state as a sacrificial agent. When two adjacent excited units underwent a one-electron transition and transferred an electron to CO_2, carbon dioxide was reduced to $HCOO^-$ in a two-electron process [97].

Jiang, Zhang, and Xiong implemented MOFs in a photocatalysis for gaseous reactions under UV light irradiation in 2014. For this purpose, the catalyst was not dissolved in an aqueous media and only interacted in its solid form with gaseous molecules. Effective molecular adsorption and activation were crucial for such a system. The authors developed a hybrid MOF-metal core–shell structure, as proven by TEM and SEM images. The microporous core of the MOF was built by $Cu_3(BTC)_2$ (BTC = benzene-1,3,5-tricarboxylate) and a semiconductor (SC) TiO_2 was included as a macroporous shell for generating excitons (Figure 15). The MOF-TiO_2 structure was referred to as $Cu_3(BTC)_2@TiO_2$. CO_2 was able to penetrate the macroporous shell structure and was captured in the microporous MOF core in which it was adsorbed on the Cu sites. The mechanism was investigated via ultrafast transient absorption. When TiO_2 was photoexcited, electron-hole pairs were formed. The electron was transferred to the $Cu_3(BTC)_2$ MOF structure including the catalytic metal atoms. Upon receiving the electrons, Cu was activated, and CO_2 reduction of adsorbed molecules took place via an eight-electron process, resulting in CH_4. The CH_4 production rate of $Cu_3(BTC)_2@TiO_2$ was determined as 2.64 $\mu mol\ g^{-1}\ h^{-1}$, whereas bare TiO_2 produced 0.52 $\mu mol\ g^{-1}\ h^{-1}\ CH_4$ and 2.29 $\mu mol\ g^{-1}\ h^{-1}\ H_2$. The MOF structure and SC improved the charge transfer from the SC to MOF and thus the charge separation within the SC [98].
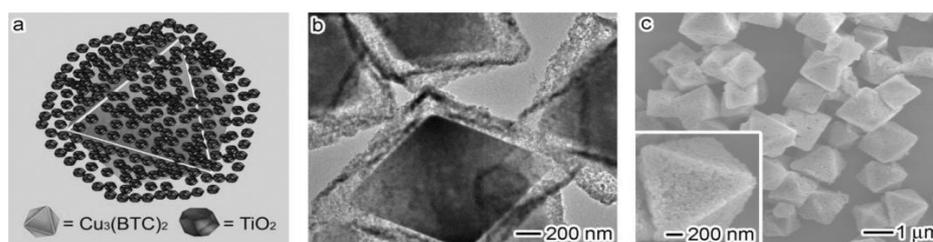
Figure 15. (**a**) Illustration of the core–shell structure; (**b**) TEM image; (**c**) SEM image of $Cu_3(BTC)_2$@TiO_2 structure. Reprinted with permission from Ref. [98]. Copyright 2014, Wiley-VCH.

Recent publications indicated that solely superficial layers on surfaces were involved in photoreactions due to restricted diffusion barriers [99–102]. Consequently, a new class of material has emerged which are 2D metal-organic layers (MOLs). MOLs are basically a monolayer version of MOFs, also referred to as MOF nanosheets.

In 2018, Lin et al. published the first photosensitizing MOL made from secondary Hf_{12} building units and $[Ru(bpy)_3]^{2+}$-derived dicarboxylate ligands by solvothermal reaction. Carboxylate exchange reactions enabled a modification of the Hf_{12}-Ru surface with an additional rhenium(I) or manganese(I) catalyst (Figure 16). The monolayer structure of 1.6 nm thickness was analyzed via HR-TEM, XRD and AFM measurements among others. The materials Hf_{12}-Ru-Mn or Hf_{12}-Ru-Re possessed both functionalities of a photosensitizer and metal catalyst. CO_2 photoreduction was carried out in acetonitrile after the addition of TEOA, and BNAH or 1,3-dimethyl-2-phenyl-2,3-dihydro-1H-benzo[d]imidazole (BIH) as an electron donor. Hf_{12}-Ru-Re together with BIH showed a product selectivity for CO of 98% and a TON of up to 3849 in 24 h under artificial light irradiation. Using BNAH as sacrificial electron donor the TON reached 2092 in 24 h. Remarkably, CO_2 reduction under sunlight radiation was feasible with the Hf_{12}-Ru-Re MOL and BIH and could reach a TON of 670 within 6 h of irradiation. Photophysical and electrochemical mechanism studies included methods such as phosphorescence spectroscopy, CV and differential pulse voltammetry (DPV). It revealed that the BIH reduced Hf_{12}-Ru units, acting as photosensitizing centers, which were then negatively charged enough to reduce the catalytic rhenium units (Figure 16) [103].
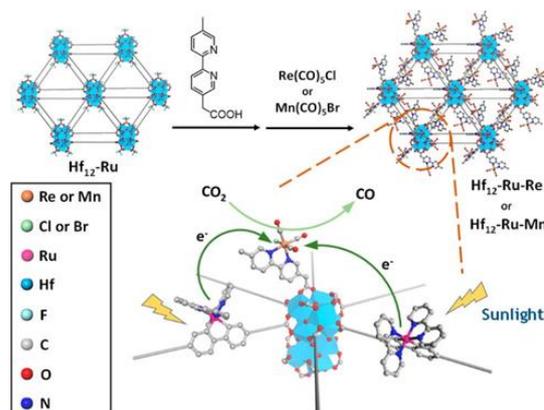

Figure 16. Schematic synthesis of Hf12-Ru-Mn and Hf12-Ru-Re and proposed sunlight-driven mechanism. Reprinted with permission from Ref. [103]. Copyright 2018, American Chemical Society.

Peng et al. reported on MOLs made from $Ni_3(HITP)_2$ (HITP = 2,3,6,7,10,11-hexaiminotriphenylene) with a planar $Ni-N_4$ coordination motif [104]. The material had been known as a semiconducting metal-organic graphene analogue with a high conductivity for charge transportation [105]. The height profile measured by AFM microscopy revealed a thickness of 4.2 nm which showed that the nanosheet was made out of only few layers of 2D MOFs. For CO_2 reduction, the MOL performed as a co-catalyst in hybrid catalytic systems under visible light irradiation with $[Ru(bpy)_3]^{2+}$ as photosensitizer and TEOA

as sacrificial agent. In a solvent mixture of water and acetonitrile, CO was formed with a selectivity of 97% and a production rate of 3450 μmol g^{-1} h^{-1}. Even after six cycles, the material proved to be stable [104]. The photocatalytic activity of $Ni_3(HITP)_2$ was further improved by adding reduced graphene oxide (rGO) that interacted with the catalyst via Coulomb interactions. The heterostructure had an impact on the electronic structure of the metal centers due to electrostatic charge transfer and π-π interactions. The CO production rate was improved to up to 3800 μmol g^{-1} h^{-1} with 92% CO selectivity. PL and PL decay, as well as ultraviolet photoelectron spectroscopy (UPS), accompanied by DFT calculations, suggested a division of the mechanistic process into three main steps: (1) photon absorbance of the photosensitizer and thus being transformed to the excited state, (2) the photosensitizer transferred its excited electron to the $Ni_3(HITP)_2$ located in the nanosheet layer, (3) CO_2 was reduced to CO at the $Ni-N_4$ sites. In detail, the photoexcited electron in the $[Ru(bpy)_3]^{2+*}$ was delocalized in the π* orbital. The formed hole was neutralized by reduction from the sacrificial electron donor TEOA. The electron was transported within the conduction band of the nanosheet to the $Ni-N_4$ sites caused by the metallicity of the MOL. $Ni-N_4$ sites acted as catalysts due to their enhanced electron density. Electrophilic adsorption of CO_2 and H^+ on catalytic $Ni-N_4$ sites was promoted. COOH* was formed as an adsorbed intermediate on the catalytic centers. Protonation of the intermediate plus reduction released H_2O and CO. The rGO enhanced the electrophilicity of $Ni-N_4$ sites and performed as an electron relay of the photogenerated electrons to the conduction band of the metal centers for reduction [106].

Gao et al. published new noble-metal-free hybrid photocatalytic nanosheets with 2D zinc(II) porphyrin-based networks of 5,10,15,20-tetrakis(4-carboxyphenyl) porphyrin (TCPP), called Zn-MOF NSs or Zn-MOLs. Photocatalytic reduction was utilized with a binuclear cobalt complex, namely $[Co_2[(OH)L](ClO_4)_3$ (L = N$[(CH_2)_2NHCH_2(m-C_6H_4)$ $CH_2NH(CH_2)]_3N$), as co-catalyst, besides TEOA as an electron donor. AFM measurements revealed a thickness of 4.7 nm of the NSs. The photocatalytic system including the co-catalyst showed a high CO selectivity of 91% and a TON of 118, which was almost twice the value compared to the bulk material of the respective Zn-MOF (TON_{CO} = 64). The Zn-MOLs proved also to be stable under visible light irradiation. The 2D network had a higher charge transport ability and thus an enhanced charge separation compared to the bulk material [107]. Based on findings from Lu et al. [108], Gao et al. proposed a mechanism for the CO_2 photoreduction to CO with Zn-MOLs (Figure 17). The building block of the Zn-MOL nanosheets, which is ZnTCPP, formed [ZnTCPP]* after being photoexcited. TEOA reduced this intermediate to [ZnTCPP]$^-$. CO_2 was coordinated to the binuclear cobalt complex containing $Co_2^{II,II}$ which formed a carbonate-bridged complex. Via proton-coupled electron transfer with the help of [ZnTCPP]$^-$, complex b was formed containing two Co centers with two different oxidation states ($Co_2^{II,III}$). After another proton-coupled electron transfer with [ZnTCPP]$^-$, c was formed containing two Co^{II} centers. Finally, CO was released, and the binuclear cobalt complex can be reintroduced in the catalytic cycle [107].
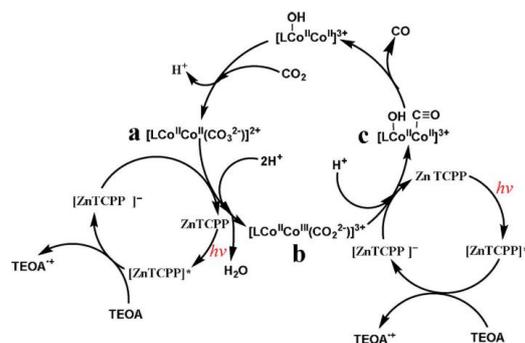

Figure 17. Proposed mechanism for the photocatalytic CO_2 reduction to CO with a Zn-MOL and $[Co_2[(OH)L](ClO_4)_3$ as co-catalyst. Reprinted with permission from Ref. [107]. Copyright 2018, Elsevier B.V.

4. Conclusions

This review summarizes the recent developments in photocatalytic CO_2 conversion using metal-containing polymers. New materials and mechanistic insights were revealed for different material classes, such as supramolecular and coordination polymers, porous organic polymers, and porous coordination polymers (MOFs and MOLs). Table 2 presents an overview of the key reports mentioned in this review.

Table 2. Overview of key reports including used catalyst system, solvent, light source and the main product after photocatalytic CO_2 reduction.

Catalyst Support	Photocatalytic System	Solvent	Light Source	Main Products	Ref.
Triblock amphiphilic micelles	Re (Cat, PS), TEOA (SA)	H_2O	500 W Xe ($\lambda \geq 400$ nm)	CO, H_2	[42]
Poly(vinyl bipyridine)	Re (Cat), Ru (PS), TEOA+BIH (SA)	DMF	green LED ($\lambda = 520 \pm 30$ nm)	CO	[44]
Polymers on quantum dots	CdS-Ni assembly (Cat, PS), TEOA (SA)	H_2O	LED ($\lambda = 420$ nm)	CO, H_2	[48]
Ullazine supramolecular polymers	Co (Cat), Chromophores (PS), TEOA (SA)	MeCN/H_2O	blue LED ($\lambda = 450$ nm)	CO, CH_4	[52]
Metal-organic coordination polymer gel	Ru (Cat), Porphyrin (PS), TEA/BNAH (SA)	MeCN/H_2O	300 W Xe lamp ($\lambda > 400$ nm)	CO, CH_4	[54]
Bipyridine COF	Re (Cat), Ir (PS), TEOA (SA)	MeCN	300 W Xe ($\lambda > 420$ nm cut-off filter)	CO, H_2	[69]
PMO with bipyridyl ligands	Ru (Cat), Ru (PS), BNAH (SA)	DMA/H_2O	500 W Hg ($\lambda > 430$ nm)	CO, $HCOO^-$	[71]
Porous CTF	Re (Cat, PS), TEOA	none	300 W Xe ($\lambda = 200$–1100 nm)	CO	[76]
HCP-TiO2-Pd	TiO2 (Cat), Pd (co-Cat)	none	300 W Xe, UV-vis light	CH_4	[83]
Metallophthalocyanine and salen POPs	Ni (Cat), Ru (PS), TEOA (SA)	MeCN/H_2O	white LED ($\lambda = 400$–800 nm)	CO	[84]
Hybrid MOF-metal core–shell structure	Cu (Cat), TiO_2 (PS)	none	300 W Xe ($\lambda < 400$ nm)	CH_4	[98]
MOLs made from $Ni_3(HITP)_2$	Ni (Cat), MOL (co-Cat), Ru (PS), TEOA (SA)	TEOA/H_2O/MeCN	100 W LED ($\lambda = 420$ nm)	CO	[104]

1D-coordination polymers were revealed to be a simple material for CO_2 reduction. Even systems without the necessity of an additional photosensitizer were already published. Moreover, supramolecular and coordination polymers are a class of efficient supports for photocatalysts. Amphiphilicity of the systems helped to prevent the degradation of the catalytic centers in an aqueous system. Additionally, self-assembled materials and hydrogels facilitated simple co-location of photosensitizer and catalysts. Proximities of the catalytic metal centers enhanced intramolecular charge transfers, but mechanistic details on new materials are still missing. Porous organic polymers that were synthesized as 3D frameworks or 2D layers performed as a versatile class of materials due to their porosity. Their tunable characteristics such as light absorption ability and energies of the band gaps were used for improvements concerning selectivity and stabilities. The field of POPs supported by non-noble metals or inorganic semiconductors, especially, was recently broadened and complemented by unraveling mechanistic details. Metal-organic frameworks have shown to have accessible pores for small molecules and can additionally already carry photocatalytically active metal centers in their basic structure. Research on this enormous variety of structures has shown that the composition of the whole system and the choice of solvent have a strong impact on carbon dioxide adsorption ability, product

selectivity, catalyst stability, productions rates, etc. In general, high electron densities and improved electron-hole separation support CH_4 formation over carbon monoxide generation. However, since both products are still C1 building blocks, photocatalyst efficiencies have to be pushed to the next level for C2 product formation.

Most of the presented photocatalytic performances have been executed in saturated CO_2 atmospheres and watery systems on a lab scale. For translation of these systems to an industrial-relevant production scale, some drawbacks need to be improved. One drawback is that the flue gas for conversion is often not pure CO_2 gas. Other gases, such as N_2, NO_2, can also be contained in the gas streams. The selectivity for CO_2 adsorption in the presence of other gas molecules on the catalytic metal centers needs to be maximized. Moreover, gas streams have rather low pressures. Efficient adsorption of carbon dioxide on catalytic active sides under low CO_2 pressure and concentrations must be facilitated for generating an industrial relevance of photocatalytic carbon dioxide reduction. As a consequence, sophisticated processes are so far only performed under laboratory utilization and need to be translated to industrial scales.

References

1. UNDP. Sustainable Development Goals: Goal 13 Climate Action. Available online: https://www1.undp.org/content/oslo-governance-centre/en/home/sustainable-development-goals/goal-13-climate-action.html (accessed on 16 May 2022).
2. Joos, F.; Spahni, R. Rates of change in natural and anthropogenic radiative forcing over the past 20,000 years. *Proc. Natl. Acad. Sci. USA* **2008**, *105*, 1425–1430. [CrossRef] [PubMed]
3. Earth's CO2 Home Page. Available online: https://www.co2.earth/ (accessed on 2 May 2022).
4. Agarwal, A.S.; Zhai, Y.; Hill, D.; Sridhar, N. The electrochemical reduction of carbon dioxide to formate/formic acid: Engineering and economic feasibility. *ChemSusChem* **2011**, *4*, 1301–1310. [CrossRef] [PubMed]
5. Meryem, S.S.; Nasreen, S.; Siddique, M.; Khan, R. An overview of the reaction conditions for an efficient photoconversion of CO_2. *Rev. Chem. Eng.* **2018**, *34*, 409–425. [CrossRef]
6. Verma, S.; Kim, B.; Jhong, H.-R.M.; Ma, S.; Kenis, P.J.A. A Gross-Margin Model for Defining Technoeconomic Benchmarks in the Electroreduction of CO_2. *ChemSusChem* **2016**, *9*, 1972–1979. [CrossRef] [PubMed]
7. Liu, M.; Pang, Y.; Zhang, B.; De Luna, P.; Voznyy, O.; Xu, J.; Zheng, X.; Dinh, C.T.; Fan, F.; Cao, C.; et al. Enhanced electrocatalytic CO_2 reduction via field-induced reagent concentration. *Nature* **2016**, *537*, 382–386. [CrossRef] [PubMed]
8. Bushuyev, O.S.; De Luna, P.; Dinh, C.T.; Tao, L.; Saur, G.; van de Lagemaat, J.; Kelley, S.O.; Sargent, E.H. What Should We Make with CO_2 and How Can We Make It? *Joule* **2018**, *2*, 825–832. [CrossRef]
9. Rosen Brian, A.; Salehi-Khojin, A.; Thorson Michael, R.; Zhu, W.; Whipple Devin, T.; Kenis Paul, J.A.; Masel Richard, I. Ionic Liquid–Mediated Selective Conversion of CO_2 to CO at Low Overpotentials. *Science* **2011**, *334*, 643–644. [CrossRef] [PubMed]
10. Zhang, S.; Kang, P.; Ubnoske, S.; Brennaman, M.K.; Song, N.; House, R.L.; Glass, J.T.; Meyer, T.J. Polyethylenimine-Enhanced Electrocatalytic Reduction of CO_2 to Formate at Nitrogen-Doped Carbon Nanomaterials. *J. Am. Chem. Soc.* **2014**, *136*, 7845–7848. [CrossRef]
11. Behera, A.; Kar, A.K.; Srivastava, R. Challenges and prospects in the selective photoreduction of CO_2 to C1 and C2 products with nanostructured materials: A review. *Mater. Horiz.* **2022**, *9*, 607–639. [CrossRef]
12. Gui, M.M.; Lee, W.P.C.; Putri, L.K.; Kong, X.Y.; Tan, L.-L.; Chai, S.-P. Photo-Driven Reduction of Carbon Dioxide: A Sustainable Approach Towards Achieving Carbon Neutrality Goal. *Front. Chem.* **2021**, *3*, 744911. [CrossRef]
13. White, J.L.; Baruch, M.F.; Pander Iii, J.E.; Hu, Y.; Fortmeyer, I.C.; Park, J.E.; Zhang, T.; Liao, K.; Gu, J.; Yan, Y.; et al. Light-Driven Heterogeneous Reduction of Carbon Dioxide: Photocatalysts and Photoelectrodes. *Chem. Rev.* **2015**, *115*, 12888–12935. [CrossRef]
14. Vu, N.N.; Kaliaguine, S.; Do, T.O. Critical Aspects and Recent Advances in Structural Engineering of Photocatalysts for Sunlight-Driven Photocatalytic Reduction of CO_2 into Fuels. *Adv. Funct. Mater.* **2019**, *29*, 1901825. [CrossRef]
15. Yoshino, S.; Takayama, T.; Yamaguchi, Y.; Iwase, A.; Kudo, A. CO2 Reduction Using Water as an Electron Donor over Heterogeneous Photocatalysts Aiming at Artificial Photosynthesis. *Acc. Chem. Res.* **2022**, *55*, 966–977. [CrossRef]

16. Qiao, J.; Liu, Y.; Hong, F.; Zhang, J. A review of catalysts for the electroreduction of carbon dioxide to produce low-carbon fuels. *Chem. Soc. Rev.* **2014**, *43*, 631–675. [CrossRef]

17. Zhu, Q.; Murphy, C.J.; Baker, L.R. Opportunities for Electrocatalytic CO_2 Reduction Enabled by Surface Ligands. *J. Am. Chem. Soc.* **2022**, *144*, 2829–2840. [CrossRef]

18. Zhu, C.; Zhao, S.; Shi, G.; Zhang, L. Structure-Function Correlation and Dynamic Restructuring of Cu for Highly Efficient Electrochemical CO_2 Conversion. *ChemSusChem* **2022**, *15*, e202200068. [CrossRef]

19. Tang, T.; Wang, Z.; Guan, J. Optimizing the Electrocatalytic Selectivity of Carbon Dioxide Reduction Reaction by Regulating the Electronic Structure of Single-Atom M-N-C Materials. *Adv. Funct. Mater.* **2022**, *32*, 2111504. [CrossRef]

20. Chen, Z.; Wang, X.; Mills, J.P.; Du, C.; Kim, J.; Wen, J.; Wu, Y.A. Two-dimensional materials for electrochemical CO_2 reduction: Materials, in situ/operando characterizations, and perspective. *Nanoscale* **2021**, *13*, 19712–19739. [CrossRef]

21. Ochedi, F.O.; Liu, D.; Yu, J.; Hussain, A.; Liu, Y. Photocatalytic, electrocatalytic and photoelectrocatalytic conversion of carbon dioxide: A review. *Environ. Chem. Lett.* **2020**, *19*, 941–967. [CrossRef]

22. Arai, T.; Sato, S.; Uemura, K.; Morikawa, T.; Kajino, T.; Motohiro, T. Photoelectrochemical reduction of CO_2 in water under visible-light irradiation by a p-type InP photocathode modified with an electropolymerized ruthenium complex. *Chem. Commun.* **2010**, *46*, 6944–6946. [CrossRef]

23. Osterloh, F.E. Inorganic nanostructures for photoelectrochemical and photocatalytic water splitting. *Chem. Soc. Rev.* **2013**, *42*, 2294–2320. [CrossRef] [PubMed]

24. Chen, C.; Kotyk, J.F.K.; Sheehan, S.W. Progress toward Commercial Application of Electrochemical Carbon Dioxide Reduction. *Chem* **2018**, *4*, 2571–2586. [CrossRef]

25. Yamazaki, Y.; Takeda, H.; Ishitani, O. Photocatalytic reduction of CO_2 using metal complexes. *J. Photochem. Photobiol. C Photochem. Rev.* **2015**, *25*, 106–137. [CrossRef]

26. Cokoja, M.; Bruckmeier, C.; Rieger, B.; Herrmann, W.A.; Kuhn, F.E. Transformation of carbon dioxide with homogeneous transition-metal catalysts: A molecular solution to a global challenge? *Angew. Chem. Int. Ed.* **2011**, *50*, 8510–8537. [CrossRef]

27. Samanta, S.; Srivastava, R. Catalytic conversion of CO_2 to chemicals and fuels: The collective thermocatalytic/photocatalytic/ electrocatalytic approach with graphitic carbon nitride. *Adv. Mater.* **2020**, *1*, 1506–1545. [CrossRef]

28. Singh, R.; Dutta, S. Integrated photocatalytic hydrogen production and pollutants or wastes treatment: Prospects and challenges. In *Sustainable Fuel Technologies Handbook*; Dutta, S., Mustansar Hussain, C., Eds.; Academic Press: Cambridge, MA, USA, 2021; pp. 541–549.

29. Zhang, Y.; Lee, T.S.; Petersen, J.L.; Milsmann, C. A Zirconium Photosensitizer with a Long-Lived Excited State: Mechanistic Insight into Photoinduced Single-Electron Transfer. *J. Am. Chem. Soc.* **2018**, *140*, 5934–5947. [CrossRef]

30. Arias-Rotondo, D.M.; McCusker, J.K. The photophysics of photoredox catalysis: A roadmap for catalyst design. *Chem. Soc. Rev.* **2016**, *45*, 5803–5820. [CrossRef]

31. Chang, X.X.; Wang, T.; Gong, J.L. CO_2 photo-reduction: Insights into CO_2 activation and reaction on surfaces of photocatalysts. *Energy Environ. Sci.* **2016**, *9*, 2177–2196. [CrossRef]

32. Gueymard, C.A. The sun's total and spectral irradiance for solar energy applications and solar radiation models. *Sol. Energy* **2004**, *76*, 423–453. [CrossRef]

33. Liu, Y.S.; Ji, G.B.; Dastageer, M.A.; Zhu, L.; Wang, J.Y.; Zhang, B.; Chang, X.F.; Gondal, M.A. Highly-active direct Z-scheme Si/TiO_2 photocatalyst for boosted CO_2 reduction into value-added methanol. *RSC Adv.* **2014**, *4*, 56961–56969. [CrossRef]

34. Lehn, J.M.; Ziessel, R. Photochemical generation of carbon monoxide and hydrogen by reduction of carbon dioxide and water under visible light irradiation. *Proc. Natl. Acad. Sci. USA* **1982**, *79*, 701–704. [CrossRef]

35. Li, K.; Peng, B.S.; Peng, T.Y. Recent Advances in Heterogeneous Photocatalytic CO_2 Conversion to Solar Fuels. *ACS Catal.* **2016**, *6*, 7485–7527. [CrossRef]

36. Shen, H.D.; Peppel, T.; Stunk, J.; Sun, Z.Y. Photocatalytic Reduction of CO_2 by Metal-Free-Based Materials: Recent Advances and Future Perspective. *Sol. RRL* **2020**, *4*, 1900546. [CrossRef]

37. Lewis, N.S.; Nocera, D.G. Powering the planet: Chemical challenges in solar energy utilization. *Proc. Natl. Acad. Sci. USA* **2006**, *103*, 15729–15735. [CrossRef]

38. Ma, Y.; Wang, Z.; Xu, X.; Wang, J. Review on porous nanomaterials for adsorption and photocatalytic conversion of CO_2. *Chin. J. Catal.* **2017**, *38*, 1956–1969. [CrossRef]

39. Batten, S.R.; Champness, N.R.; Chen, X.-M.; Garcia-Martinez, J.; Kitagawa, S.; Öhrström, L.; O'Keeffe, M.; Suh, M.P.; Reedijk, J. Coordination polymers, metal–organic frameworks and the need for terminology guidelines. *CrystEngComm* **2012**, *14*, 3001–3004. [CrossRef]

40. Batten, S.R.; Champness, N.R.; Chen, X.-M.; Garcia-Martinez, J.; Kitagawa, S.; Öhrström, L.; O'Keeffe, M.; Paik Suh, M.; Reedijk, J. Terminology of metal–organic frameworks and coordination polymers (IUPAC Recommendations 2013). *Pure Appl. Chem.* **2013**, *85*, 1715–1724. [CrossRef]

41. Adams, F.; Pschenitza, M.; Rieger, B. Yttrium-Catalyzed Synthesis of Bipyridine-Functionalized AB-Block Copolymers: Micellar Support for Photocatalytic Active Rhenium-Complexes. *ChemCatChem* **2018**, *10*, 4309–4316. [CrossRef]

42. Ren, F.Y.; Chen, K.; Qiu, L.Q.; Chen, J.M.; Darensbourg, D.J.; He, L.N. Amphiphilic Polycarbonate Micellar Rhenium Catalysts for Efficient Photocatalytic CO_2 Reduction in Aqueous Media. *Angew. Chem. Int. Ed.* **2022**, *134*, e202200751. [CrossRef]

43. Deacy, A.C.; Moreby, E.; Phanopoulos, A.; Williams, C.K. Co(III)/Alkali-Metal(I) Heterodinuclear Catalysts for the Ring-Opening Copolymerization of CO_2 and Propylene Oxide. *J. Am. Chem. Soc.* **2020**, *142*, 19150–19160. [CrossRef]

44. Maier, A.S.; Thomas, C.; Kränzlein, M.; Pehl, T.M.; Rieger, B. Macromolecular Rhenium–Ruthenium Complexes for Photocatalytic CO_2 Conversion: From Catalytic Lewis Pair Polymerization to Well-Defined Poly(vinyl bipyridine)–Metal Complexes. *Macromolecules* **2022**. [CrossRef]

45. Lee, S.; Kim, S.; Park, C.; Moon, G.H.; Son, H.J.; Baeg, J.O.; Kim, W.; Choi, W. Nafion-Assisted Noncovalent Assembly of Molecular Sensitizers and Catalysts for Sustained Photoreduction of CO_2 to CO. *ACS Sustain. Chem. Eng* **2020**, *8*, 3709–3717. [CrossRef]

46. Mauritz, K.A.; Moore, R.B. State of understanding of nafion. *Chem. Rev.* **2004**, *104*, 4535–4585. [CrossRef] [PubMed]

47. Orchanian, N.M.; Hong, L.E.; Skrainka, J.A.; Esterhuizen, J.A.; Popov, D.A.; Marinescu, S.C. Surface-Immobilized Conjugated Polymers Incorporating Rhenium Bipyridine Motifs for Electrocatalytic and Photocatalytic CO_2 Reduction. *ACS Appl. Energy Mater.* **2018**, *2*, 110–123. [CrossRef]

48. Wang, H.Y.; Xie, W.H.; Wei, D.D.; Hu, R.; Wang, N.; Chang, K.; Lei, S.L.; Wang, B.; Cao, R. A Hybrid Assembly with Nickel Poly-Pyridine Polymer on CdS Quantum Dots for Photo-Reducing CO_2 into Syngas with Controlled H_2/CO Ratios. *ChemSusChem* **2022**, *15*, e202200200. [CrossRef]

49. Wang, J.J.; Li, Z.J.; Li, X.B.; Fan, X.B.; Meng, Q.Y.; Yu, S.; Li, C.B.; Li, J.X.; Tung, C.H.; Wu, L.Z. Photocatalytic hydrogen evolution from glycerol and water over nickel-hybrid cadmium sulfide quantum dots under visible-light irradiation. *ChemSusChem* **2014**, *7*, 1468–1475. [CrossRef]

50. Otsuki, J. Supramolecular approach towards light-harvesting materials based on porphyrins and chlorophylls. *J. Mater. Chem. A* **2018**, *6*, 6710–6753. [CrossRef]

51. Hestand, N.J.; Kazantsev, R.V.; Weingarten, A.S.; Palmer, L.C.; Stupp, S.I.; Spano, F.C. Extended-Charge-Transfer Excitons in Crystalline Supramolecular Photocatalytic Scaffolds. *J. Am. Chem. Soc.* **2016**, *138*, 11762–11774. [CrossRef]

52. Dumele, O.; Dordevic, L.; Sai, H.; Cotey, T.J.; Sangji, M.H.; Sato, K.; Dannenhoffer, A.J.; Stupp, S.I. Photocatalytic Aqueous CO_2 Reduction to CO and CH_4 Sensitized by Ullazine Supramolecular Polymers. *J. Am. Chem. Soc.* **2022**, *144*, 3127–3136. [CrossRef]

53. Park, S.; Lim, J.H.; Chung, S.W.; Mirkin, C.A. Self-assembly of mesoscopic metal-polymer amphiphiles. *Science* **2004**, *303*, 348–351. [CrossRef]

54. Verma, P.; Rahimi, F.A.; Samanta, D.; Kundu, A.; Dasgupta, J.; Maji, T.K. Visible-Light-Driven Photocatalytic CO_2 Reduction to CO/CH_4 Using a Metal-Organic "Soft" Coordination Polymer Gel. *Angew. Chem. Int. Ed.* **2022**, *61*, e202116094. [CrossRef]

55. Goze, C.; Sabatini, C.; Barbieri, A.; Barigelletti, F.; Ziessel, R. Ruthenium-terpyridine complexes with multiple ethynylpyrenyl or ethynyltoluyl subunits: X-ray structure, redox, and spectroscopic properties. *Inorg. Chem.* **2007**, *46*, 7341–7350. [CrossRef]

56. Kuramochi, Y.; Ishitani, O.; Ishida, H. Reaction mechanisms of catalytic photochemical CO_2 reduction using Re(I) and Ru(II) complexes. *Coord. Chem. Rev.* **2018**, *373*, 333–356. [CrossRef]

57. Liu, Y.; Guo, J.H.; Dao, X.Y.; Zhang, X.D.; Zhao, Y.; Sun, W.Y. Coordination polymers with a pyridyl-salen ligand for photocatalytic carbon dioxide reduction. *Chem. Commun.* **2020**, *56*, 4110–4113. [CrossRef]

58. Costentin, C.; Sayeant, J.M.; Tard, C. Catalysis of CO_2 Electrochemical Reduction by Protonated Pyridine and Similar Molecules. Useful Lessons from a Methodological Misadventure. *ACS Energy Lett.* **2018**, *3*, 695–703. [CrossRef]

59. Cole, E.B.; Lakkaraju, P.S.; Rampulla, D.M.; Morris, A.J.; Abelev, E.; Bocarsly, A.B. Using a one-electron shuttle for the multielectron reduction of CO_2 to methanol: Kinetic, mechanistic, and structural insights. *J. Am. Chem. Soc.* **2010**, *132*, 11539–11551. [CrossRef]

60. Dridi, H.; Comminges, C.; Morais, C.; Meledje, J.C.; Kokoh, K.B.; Costentin, C.; Saveant, J.M. Catalysis and Inhibition in the Electrochemical Reduction of CO_2 on Platinum in the Presence of Protonated Pyridine. New Insights into Mechanisms and Products. *J. Am. Chem. Soc.* **2017**, *139*, 13922–13928. [CrossRef]

61. Benseghir, Y.; Solé-Daura, A.; Mialane, P.; Marrot, J.; Dalecky, L.; Béchu, S.; Frégnaux, M.; Gomez-Mingot, M.; Fontecave, M.; Mellot-Draznieks, C.; et al. Understanding the Photocatalytic Reduction of CO_2 with Heterometallic Molybdenum(V) Phosphate Polyoxometalates in Aqueous Media. *ACS Catal.* **2021**, *12*, 453–464. [CrossRef]

62. Cheng, Y.Z.; Ding, X.S.; Han, B.H. Porous Organic Polymers for Photocatalytic Carbon Dioxide Reduction. *ChemPhotoChem* **2021**, *5*, 406–417. [CrossRef]

63. Liu, M.Y.; Guo, L.P.; Jin, S.B.; Tan, B.E. Covalent triazine frameworks: Synthesis and applications. *J. Mater. Chem. A* **2019**, *7*, 5153–5172. [CrossRef]

64. Lu, M.; Zhang, M.; Liu, J.; Chen, Y.; Liao, J.P.; Yang, M.Y.; Cai, Y.P.; Li, S.L.; Lan, Y.Q. Covalent Organic Framework Based Functional Materials: Important Catalysts for Efficient CO_2 Utilization. *Angew. Chem. Int. Ed.* **2022**, *61*, e202200003. [CrossRef] [PubMed]

65. Thornton, A.W.; Winkler, D.A.; Liu, M.S.; Haranczyk, M.; Kennedy, D.F. Towards computational design of zeolite catalysts for CO_2 reduction. *RSC Adv.* **2015**, *5*, 44361–44370. [CrossRef]

66. Auerbach, S.M.; Carrado, K.A.; Dutta, P.K. *Handbook of Zeolite Science and Technology*; CRC Press: Boca Raton, FL, USA, 2003.

67. Geng, K.; He, T.; Liu, R.; Dalapati, S.; Tan, K.T.; Li, Z.; Tao, S.; Gong, Y.; Jiang, Q.; Jiang, D. Covalent Organic Frameworks: Design, Synthesis, and Functions. *Chem. Rev.* **2020**, *120*, 8814–8933. [CrossRef] [PubMed]

68. Liang, H.P.; Acharjya, A.; Anito, D.A.; Vogl, S.; Wang, T.X.; Thomas, A.; Han, B.H. Rhenium-Metalated Polypyridine-Based Porous Polycarbazoles for Visible-Light CO_2 Photoreduction. *ACS Catal.* **2019**, *9*, 3959–3968. [CrossRef]

69. Fu, Z.; Wang, X.; Gardner, A.M.; Wang, X.; Chong, S.Y.; Neri, G.; Cowan, A.J.; Liu, L.; Li, X.; Vogel, A.; et al. A stable covalent organic framework for photocatalytic carbon dioxide reduction. *Chem. Sci.* **2020**, *11*, 543–550. [CrossRef]

70. Yang, S.; Hu, W.; Zhang, X.; He, P.; Pattengale, B.; Liu, C.; Cendejas, M.; Hermans, I.; Zhang, X.; Zhang, J.; et al. 2D Covalent Organic Frameworks as Intrinsic Photocatalysts for Visible Light-Driven CO_2 Reduction. *J. Am. Chem. Soc.* **2018**, *140*, 14614–14618. [CrossRef]

71. Kuramochi, Y.; Sekine, M.; Kitamura, K.; Maegawa, Y.; Goto, Y.; Shirai, S.; Inagaki, S.; Ishida, H. Photocatalytic CO_2 Reduction by Periodic Mesoporous Organosilica (PMO) Containing Two Different Ruthenium Complexes as Photosensitizing and Catalytic Sites. *Chem. Eur. J.* **2017**, *23*, 10301–10309. [CrossRef]

72. Lu, M.; Liu, J.; Li, Q.; Zhang, M.; Liu, M.; Wang, J.L.; Yuan, D.Q.; Lan, Y.Q. Rational Design of Crystalline Covalent Organic Frameworks for Efficient CO_2 Photoreduction with H_2O. *Angew. Chem. Int. Ed.* **2019**, *58*, 12392–12397. [CrossRef]

73. Lv, H.; Sa, R.; Li, P.; Yuan, D.; Wang, X.; Wang, R. Metalloporphyrin-based covalent organic frameworks composed of the electron donor-acceptor dyads for visible-light-driven selective CO_2 reduction. *Sci. China Chem.* **2020**, *63*, 1289–1294. [CrossRef]

74. Zhong, W.; Sa, R.; Li, L.; He, Y.; Li, L.; Bi, J.; Zhuang, Z.; Yu, Y.; Zou, Z. A Covalent Organic Framework Bearing Single Ni Sites as a Synergistic Photocatalyst for Selective Photoreduction of CO_2 to CO. *J. Am. Chem. Soc.* **2019**, *141*, 7615–7621. [CrossRef]

75. Wang, W.Y.; Xi, Y.; Yang, C.; Byun, J.; Cheng, J.J.; Wang, S.B.; Wang, X.C. Incorporation of Metal Active Sites on Porous Polycarbazoles for Photocatalytic CO_2 Reduction. *ChemCatChem* **2022**, *14*, e202101872. [CrossRef]

76. Xu, R.; Wang, X.S.; Zhao, H.; Lin, H.; Huang, Y.B.; Cao, R. Rhenium-modified porous covalent triazine framework for highly efficient photocatalytic carbon dioxide reduction in a solid-gas system. *Catal. Sci. Technol.* **2018**, *8*, 2224–2230. [CrossRef]

77. Thomas, A. Functional materials: From hard to soft porous frameworks. *Angew. Chem. Int. Ed.* **2010**, *49*, 8328–8344. [CrossRef]

78. Kuhn, P.; Thomas, A.; Antonietti, M. Toward Tailorable Porous Organic Polymer Networks: A High-Temperature Dynamic Polymerization Scheme Based on Aromatic Nitriles. *Macromolecules* **2009**, *42*, 319–326. [CrossRef]

79. Liu, W.; Li, X.; Wang, C.; Pan, H.; Liu, W.; Wang, K.; Zeng, Q.; Wang, R.; Jiang, J. A Scalable General Synthetic Approach toward Ultrathin Imine-Linked Two-Dimensional Covalent Organic Framework Nanosheets for Photocatalytic CO_2 Reduction. *J. Am. Chem. Soc.* **2019**, *141*, 17431–17440. [CrossRef]

80. Wang, S.; Xu, M.; Peng, T.; Zhang, C.; Li, T.; Hussain, I.; Wang, J.; Tan, B. Porous hypercrosslinked polymer-TiO_2-graphene composite photocatalysts for visible-light-driven CO_2 conversion. *Nat. Commun.* **2019**, *10*, 676. [CrossRef]

81. Gu, L.; Wang, J.; Cheng, H.; Zhao, Y.; Liu, L.; Han, X. One-step preparation of graphene-supported anatase TiO_2 with exposed {001} facets and mechanism of enhanced photocatalytic properties. *ACS Appl. Mater. Interfaces* **2013**, *5*, 3085–3093. [CrossRef]

82. Wang, S.; Zhang, C.; Shu, Y.; Jiang, S.; Xia, Q.; Chen, L.; Jin, S.; Hussain, I.; Cooper, A.I.; Tan, B. Layered microporous polymers by solvent knitting method. *Sci. Adv.* **2017**, *3*, e1602610. [CrossRef]

83. Zhan, Z.; Wang, H.; Huang, Q.; Li, S.; Yi, X.; Tang, Q.; Wang, J.; Tan, B. Grafting Hypercrosslinked Polymers on TiO_2 Surface for Anchoring Ultrafine Pd Nanoparticles: Dramatically Enhanced Efficiency and Selectivity toward Photocatalytic Reduction of CO_2 to CH_4. *Small* **2022**, *18*, e2105083. [CrossRef]

84. Dong, X.Y.; Si, Y.N.; Wang, Q.Y.; Wang, S.; Zang, S.Q. Integrating Single Atoms with Different Microenvironments into One Porous Organic Polymer for Efficient Photocatalytic CO_2 Reduction. *Adv. Mater.* **2021**, *33*, e2101568. [CrossRef]

85. Huang, N.; Lee, K.H.; Yue, Y.; Xu, X.; Irle, S.; Jiang, Q.; Jiang, D. A Stable and Conductive Metallophthalocyanine Framework for Electrocatalytic Carbon Dioxide Reduction in Water. *Angew. Chem. Int. Ed.* **2020**, *59*, 16587–16593. [CrossRef] [PubMed]

86. Zhang, M.D.; Si, D.H.; Yi, J.D.; Yin, Q.; Huang, Y.B.; Cao, R. Conductive phthalocyanine-based metal-organic framework as a highly efficient electrocatalyst for carbon dioxide reduction reaction. *Sci. China Chem.* **2021**, *64*, 1332–1339. [CrossRef]

87. Kuila, A.; Surib, N.A.; Mishra, N.S.; Nawaz, A.; Leong, K.H.; Sim, L.C.; Saravanan, P.; Ibrahim, S. Metal Organic Frameworks: A New Generation Coordination Polymers for Visible Light Photocatalysis. *ChemistrySelect* **2017**, *2*, 6163–6177. [CrossRef]

88. Furukawa, H.; Cordova, K.E.; O'Keeffe, M.; Yaghi, O.M. The chemistry and applications of metal-organic frameworks. *Science* **2013**, *341*, 1230444. [CrossRef]

89. Moosavi, S.M.; Nandy, A.; Jablonka, K.M.; Ongari, D.; Janet, J.P.; Boyd, P.G.; Lee, Y.; Smit, B.; Kulik, H.J. Understanding the diversity of the metal-organic framework ecosystem. *Nat. Commun.* **2020**, *11*, 4068. [CrossRef]

90. Dao, X.Y.; Sun, W.Y. Single- and mixed-metal-organic framework photocatalysts for carbon dioxide reduction. *Inorg. Chem. Front.* **2021**, *8*, 3178–3204. [CrossRef]

91. Kidanemariam, A.; Lee, J.; Park, J. Recent Innovation of Metal-Organic Frameworks for Carbon Dioxide Photocatalytic Reduction. *Polymers* **2019**, *11*, 2090. [CrossRef]

92. Redfern, L.R.; Farha, O.K. Mechanical properties of metal-organic frameworks. *Chem. Sci.* **2019**, *10*, 10666–10679. [CrossRef]

93. Santaclara, J.G.; Nasalevich, M.A.; Castellanos, S.; Evers, W.H.; Spoor, F.C.; Rock, K.; Siebbeles, L.D.; Kapteijn, F.; Grozema, F.; Houtepen, A.; et al. Organic Linker Defines the Excited-State Decay of Photocatalytic MIL-125(Ti)-Type Materials. *ChemSusChem* **2016**, *9*, 388–395. [CrossRef]

94. Lu, G.; Li, S.; Guo, Z.; Farha, O.K.; Hauser, B.G.; Qi, X.; Wang, Y.; Wang, X.; Han, S.; Liu, X.; et al. Imparting functionality to a metal-organic framework material by controlled nanoparticle encapsulation. *Nat. Chem.* **2012**, *4*, 310–316. [CrossRef]

95. Maina, J.W.; Pozo-Gonzalo, C.; Kong, L.X.; Schutz, J.; Hill, M.; Dumee, L.F. Metal organic framework based catalysts for CO_2 conversion. *Mater. Horiz.* **2017**, *4*, 345–361. [CrossRef]

96. Rowsell, J.L.C.; Yaghi, O.M. Metal-organic frameworks: A new class of porous materials. *Microporous Mesoporous Mater.* **2004**, *73*, 3–14. [CrossRef]

97. Li, L.; Zhang, S.; Xu, L.; Wang, J.; Shi, L.-X.; Chen, Z.-N.; Hong, M.; Luo, J. Effective visible-light driven CO_2 photoreduction via a promising bifunctional iridium coordination polymer. *Chem. Sci.* **2014**, *5*, 3808–3813. [CrossRef]

98. Li, R.; Hu, J.; Deng, M.; Wang, H.; Wang, X.; Hu, Y.; Jiang, H.L.; Jiang, J.; Zhang, Q.; Xie, Y.; et al. Integration of an inorganic semiconductor with a metal-organic framework: A platform for enhanced gaseous photocatalytic reactions. *Adv. Mater.* **2014**, *26*, 4783–4788. [CrossRef]

99. Lin, Z.; Thacker, N.C.; Sawano, T.; Drake, T.; Ji, P.; Lan, G.; Cao, L.; Liu, S.; Wang, C.; Lin, W. Metal-organic layers stabilize earth-abundant metal-terpyridine diradical complexes for catalytic C-H activation. *Chem. Sci.* **2018**, *9*, 143–151. [CrossRef]

100. Zhao, M.; Wang, Y.; Ma, Q.; Huang, Y.; Zhang, X.; Ping, J.; Zhang, Z.; Lu, Q.; Yu, Y.; Xu, H.; et al. Ultrathin 2D Metal-Organic Framework Nanosheets. *Adv. Mater.* **2015**, *27*, 7372–7378. [CrossRef]

101. Lan, G.; Ni, K.; Xu, R.; Lu, K.; Lin, Z.; Chan, C.; Lin, W. Nanoscale Metal-Organic Layers for Deeply Penetrating X-ray-Induced Photodynamic Therapy. *Angew. Chem. Int. Ed.* **2017**, *56*, 12102–12106. [CrossRef]

102. Cao, L.; Lin, Z.; Peng, F.; Wang, W.; Huang, R.; Wang, C.; Yan, J.; Liang, J.; Zhang, Z.; Zhang, T.; et al. Self-Supporting Metal-Organic Layers as Single-Site Solid Catalysts. *Angew. Chem. Int. Ed.* **2016**, *55*, 4962–4966. [CrossRef]

103. Lan, G.; Li, Z.; Veroneau, S.S.; Zhu, Y.Y.; Xu, Z.; Wang, C.; Lin, W. Photosensitizing Metal-Organic Layers for Efficient Sunlight-Driven Carbon Dioxide Reduction. *J. Am. Chem. Soc.* **2018**, *140*, 12369–12373. [CrossRef]

104. Zhu, W.; Zhang, C.F.; Li, Q.; Xiong, L.K.; Chen, R.X.; Wan, X.B.; Wang, Z.; Chen, W.; Deng, Z.; Peng, Y. Selective reduction of CO_2 by conductive MOF nanosheets as an efficient co-catalyst under visible light illumination. *Appl. Catal. B* **2018**, *238*, 339–345. [CrossRef]

105. Sheberla, D.; Sun, L.; Blood-Forsythe, M.A.; Er, S.; Wade, C.R.; Brozek, C.K.; Aspuru-Guzik, A.; Dinca, M. High electrical conductivity in Ni(3)(2,3,6,7,10,11-hexaiminotriphenylene)(2), a semiconducting metal-organic graphene analogue. *J. Am. Chem. Soc.* **2014**, *136*, 8859–8862. [CrossRef] [PubMed]

106. Mu, Q.Q.; Zhu, W.; Li, X.; Zhang, C.F.; Su, Y.H.; Lian, Y.B.; Qi, P.W.; Deng, Z.; Zhang, D.; Wang, S.; et al. Electrostatic charge transfer for boosting the photocatalytic CO2 reduction on metal centers of 2D MOF/rGO heterostructure. *Appl. Catal. B* **2020**, *262*, 118144. [CrossRef]

107. Ye, L.; Gao, Y.; Cao, S.Y.; Chen, H.; Yao, Y.; Hou, J.G.; Sun, L.C. Assembly of highly efficient photocatalytic CO2 conversion systems with ultrathin two-dimensional metal-organic framework nanosheets. *Appl. Catal. B* **2018**, *227*, 54–60. [CrossRef]

108. Ouyang, T.; Huang, H.H.; Wang, J.W.; Zhong, D.C.; Lu, T.B. A Dinuclear Cobalt Cryptate as a Homogeneous Photocatalyst for Highly Selective and Efficient Visible-Light Driven CO_2 Reduction to CO in $CH_3 CN/H_2 O$ Solution. *Angew. Chem. Int. Ed.* **2017**, *56*, 738–743. [CrossRef]